New figure numbers given, with old figure numbers in brackets

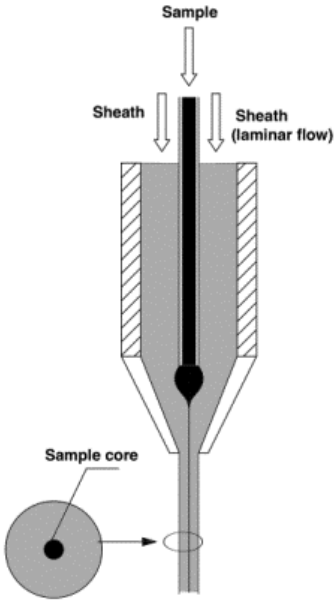

Ch I S1 Figure 1 (1): Sample core after hydrodynamic focussing by laminar sheath flow in a flow chamber

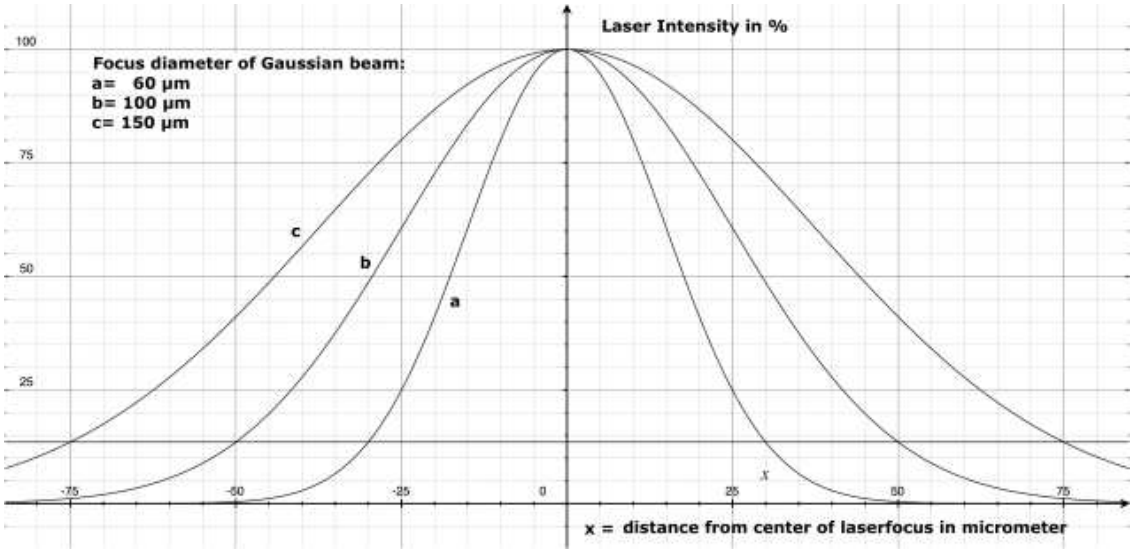

Ch I S1 Figure 2 (2): Intensity profile of a focus spot of a Gaussian laser beam.

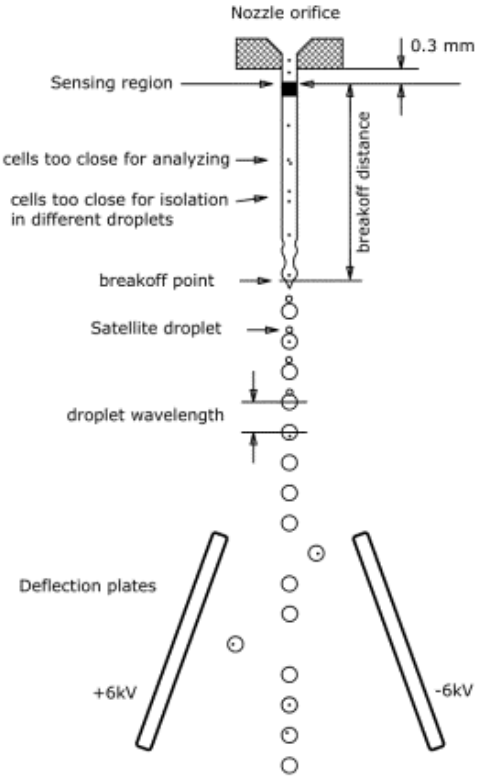

Ch I S1 Figure 3 (3): Liquid stream of a jet in air sensing cell sorter.

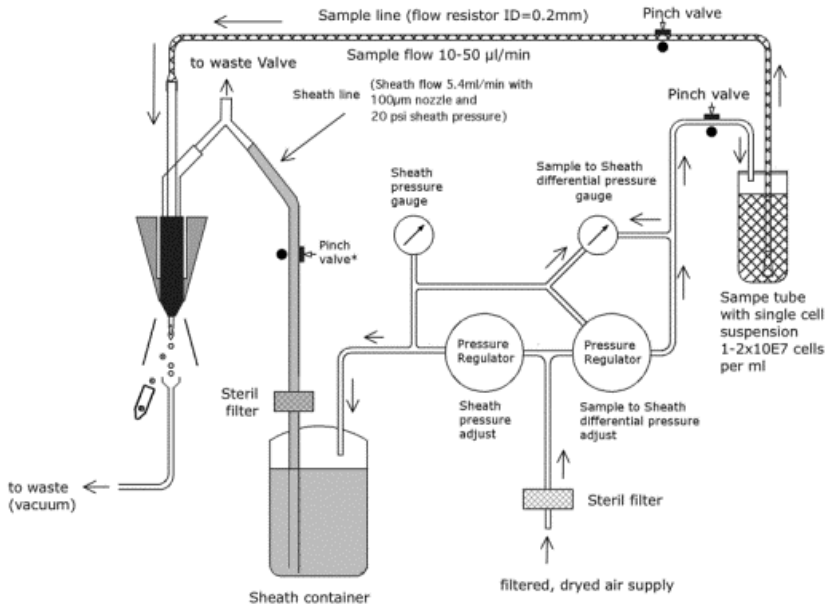

Ch I S1 Figure 4 (4): Schematics of fluidics of a jet in air sensing cell sorter

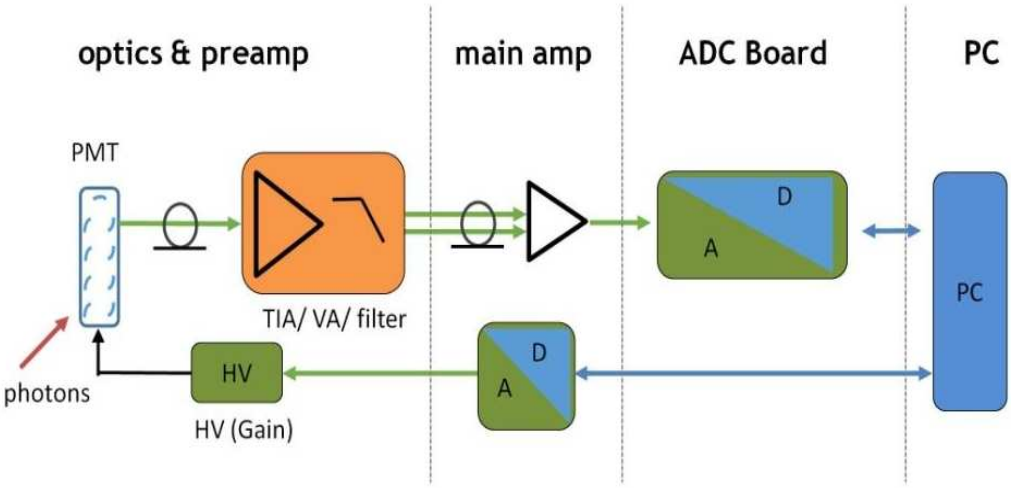

Ch I S2 Figure 5 (1): Typical electronic signal processing of a flow cytometer.

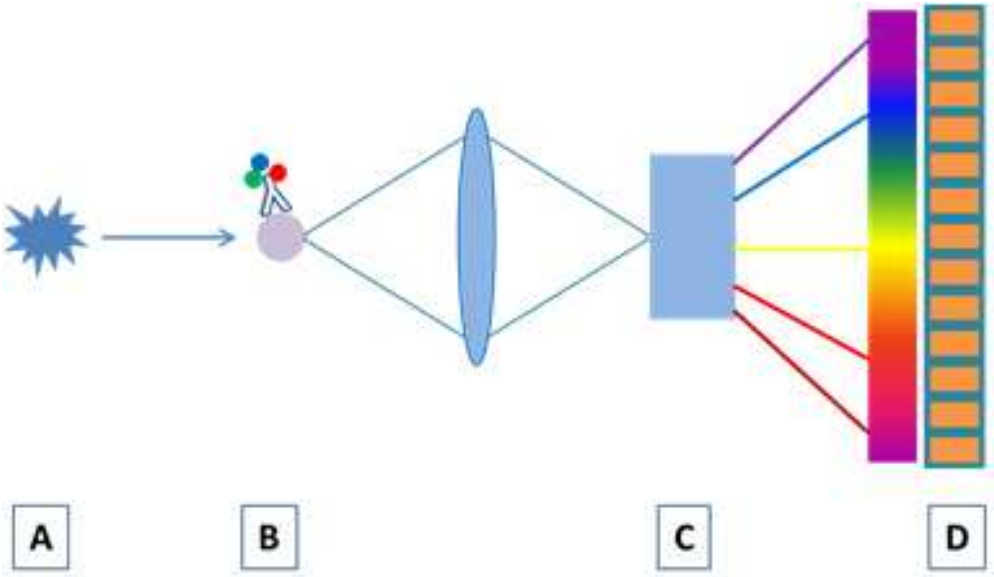

Ch I S3 Figure 6 (1): Principle of a spectral flow cytometer.

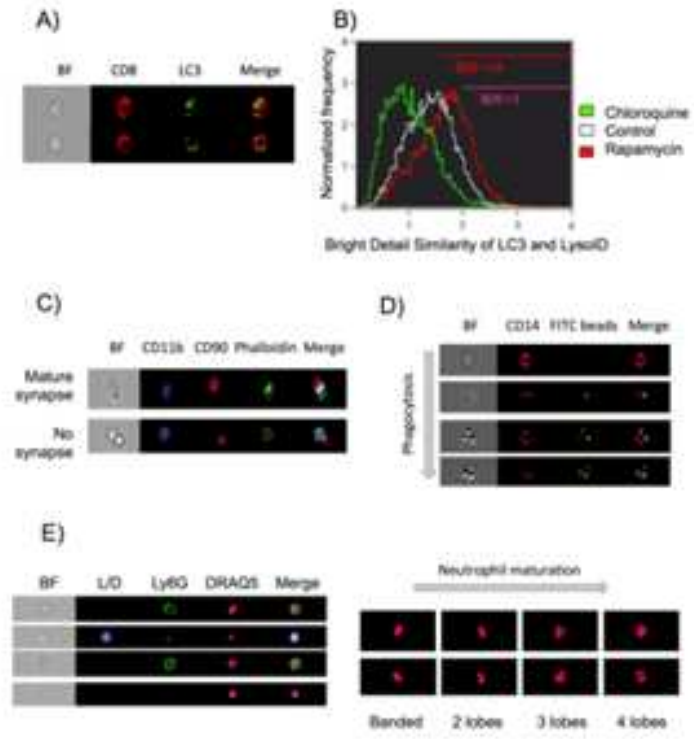

Ch I S4 Figure 7 (1): Amnis® ImageStream assays on immune cells.

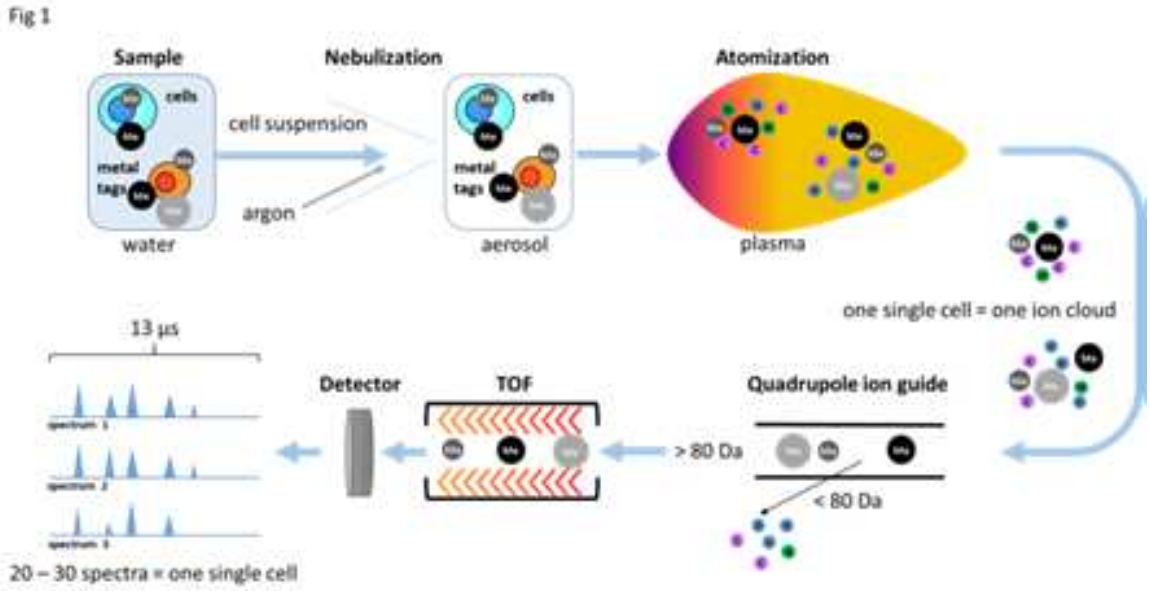

Ch I S5 Figure 8 (1). Schematic overview of a mass cytometric measurement.

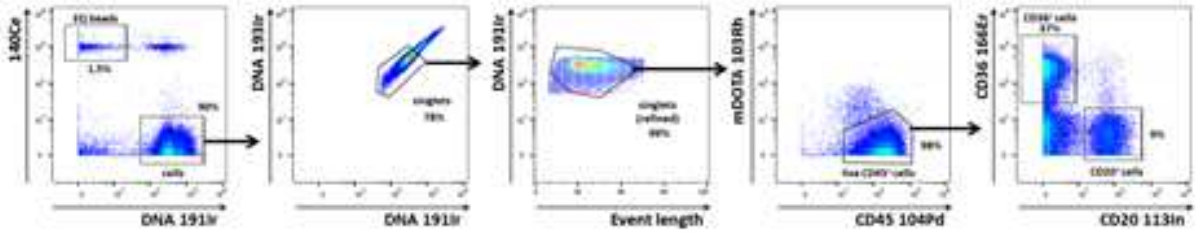

Ch I S5 Figure 9 (2). Typical gating strategy for PBMC analyzed by mass cytometry

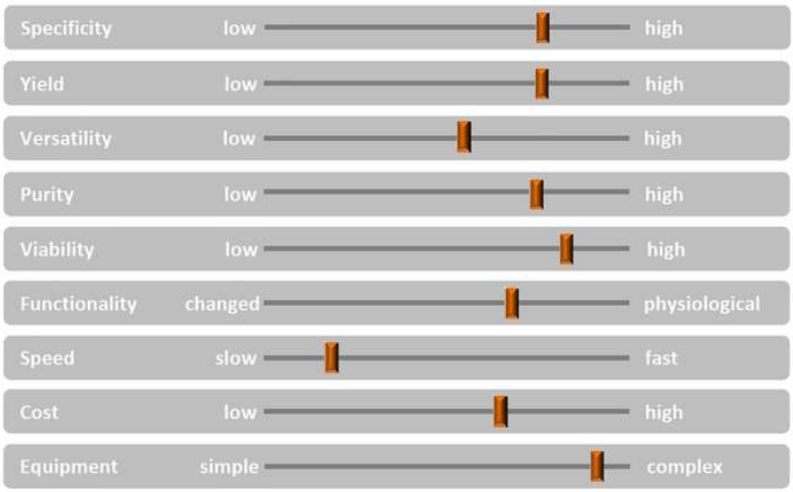

Ch II S1 Figure 10 (1): Check-list: parameters for selecting a sorting method

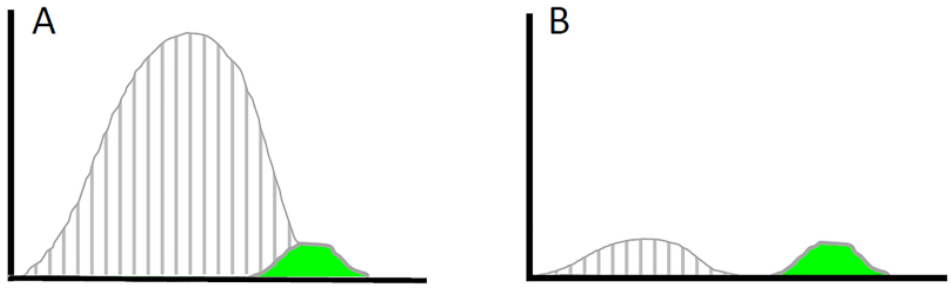

Ch II S1 Figure 11 (2): Improvement of population discrimination after pre-enrichment.

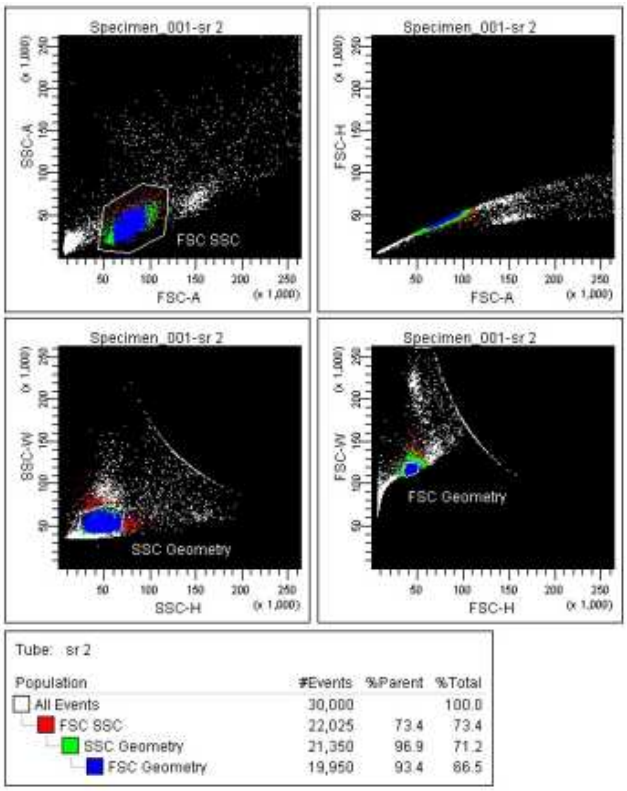

Ch II S2.1 Figure 12 (1): PBMC Sort.

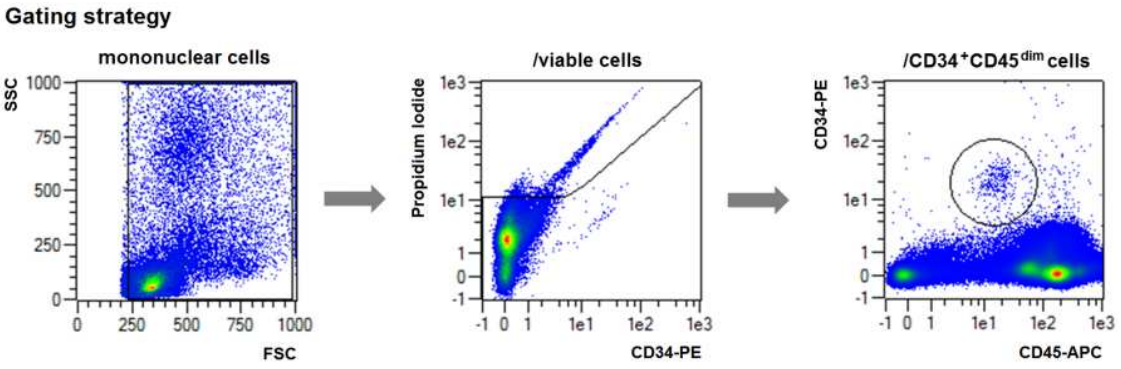

Ch II S2.2 Figure 13 (1): Staining pattern and gating strategy for a CD34+ enrichment.

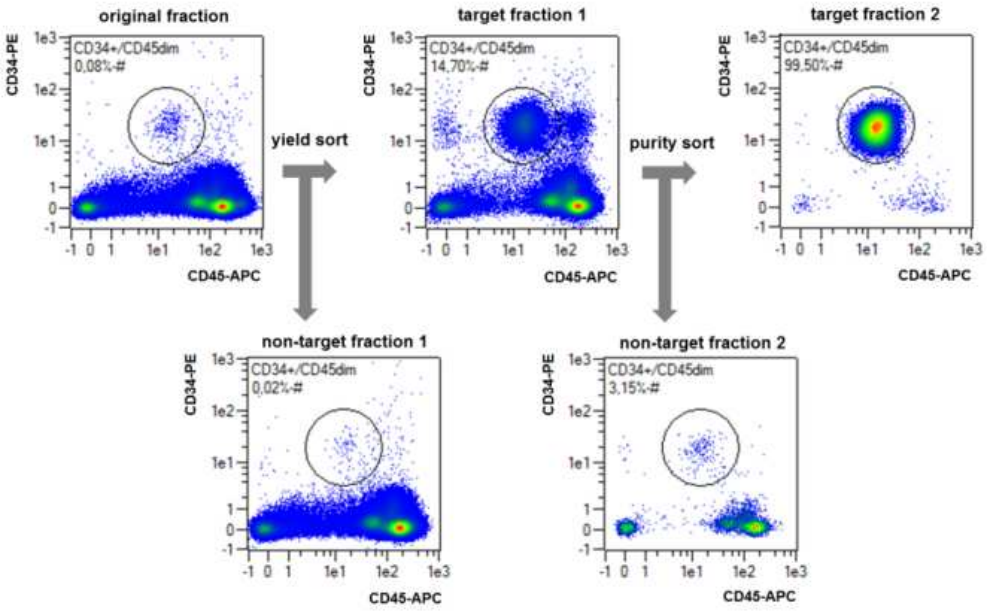

Ch II S2.2 Figure 14 (2): Result of a sequential sorting process.

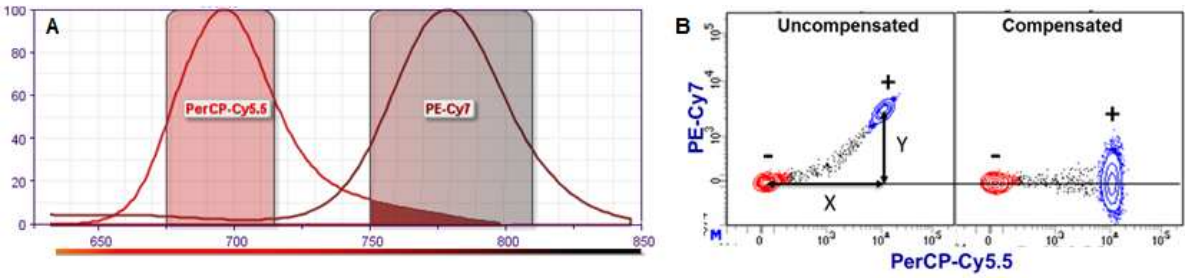

Ch III S1 Figure 15 (1): Spillover and compensation.

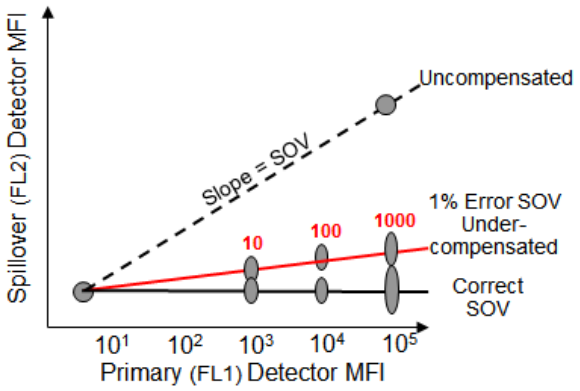

Ch III S1 Figure 16 (2): Brightness of positive population.

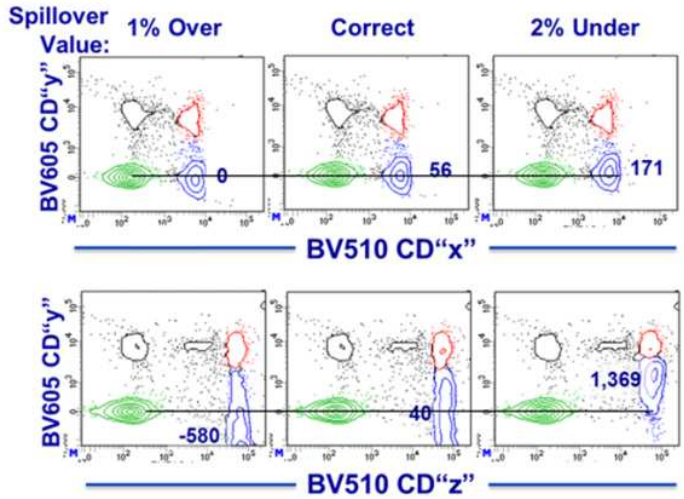

Ch III S1 Figure 17 (3): Accuracy for SOV.

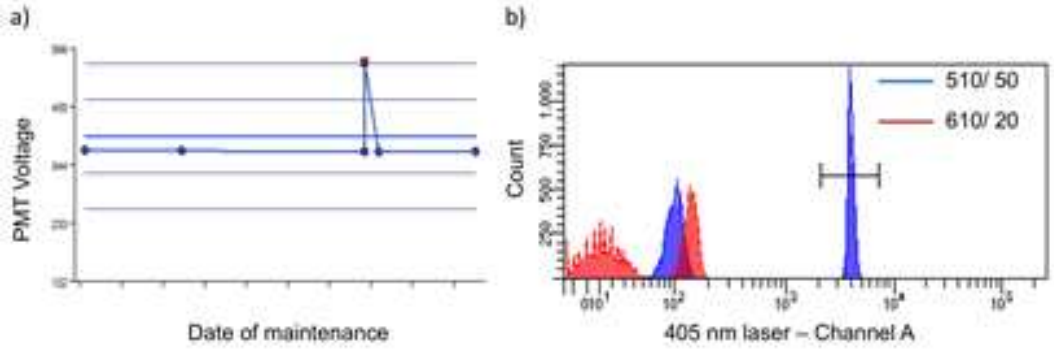

Ch III S2 Figure 18 (1): Examples for performance tracking with and without a CS&T module, performed according to [1].

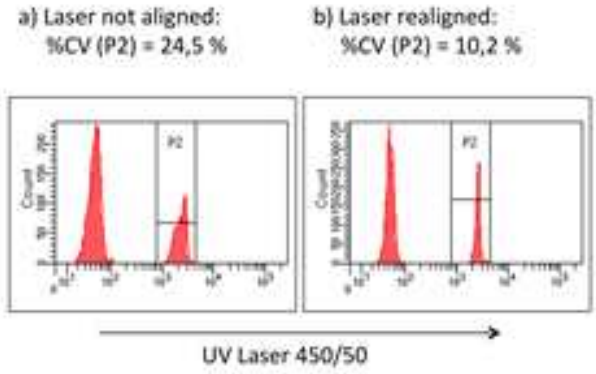

Ch III S2 Figure 19 (2): How one can detect suboptimal alignment of lasers.

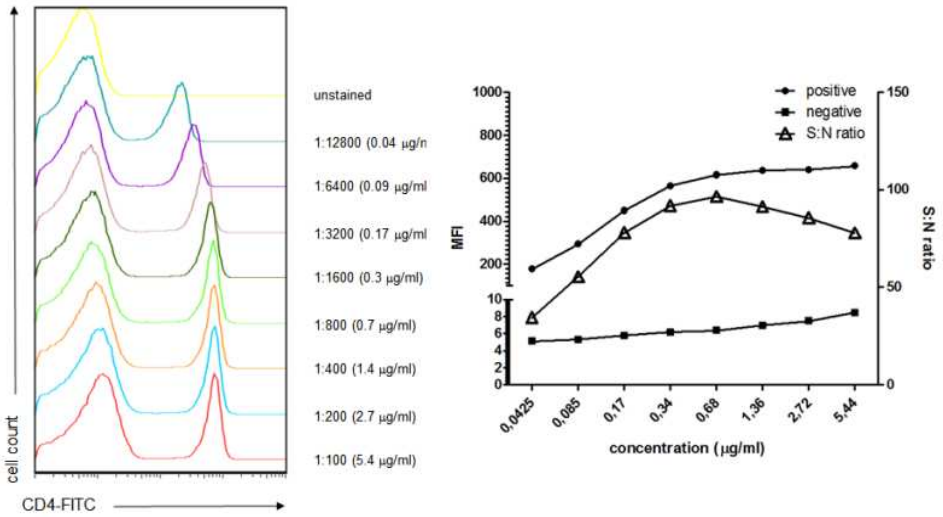

Ch IV S2 Figure 20 (1): Titration of a CD4 mAb (clone GK1.5) conjugated to FITC and titrated on murine splenocytes.

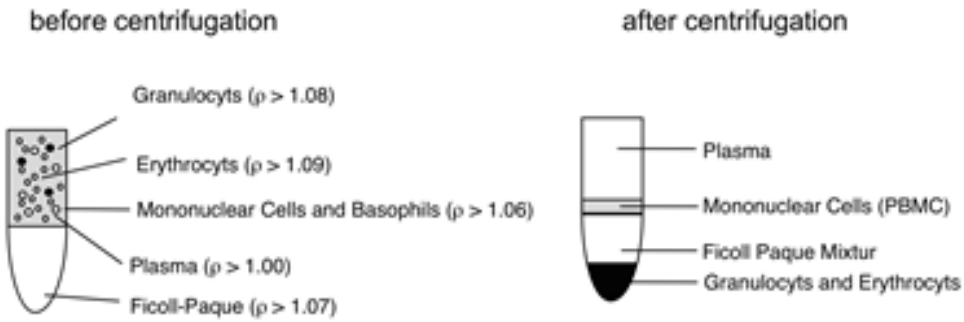

Ch IV S4 Figure 21 (1): Schemata of density gradient centrifugation with Ficoll® as pre-enrichment.

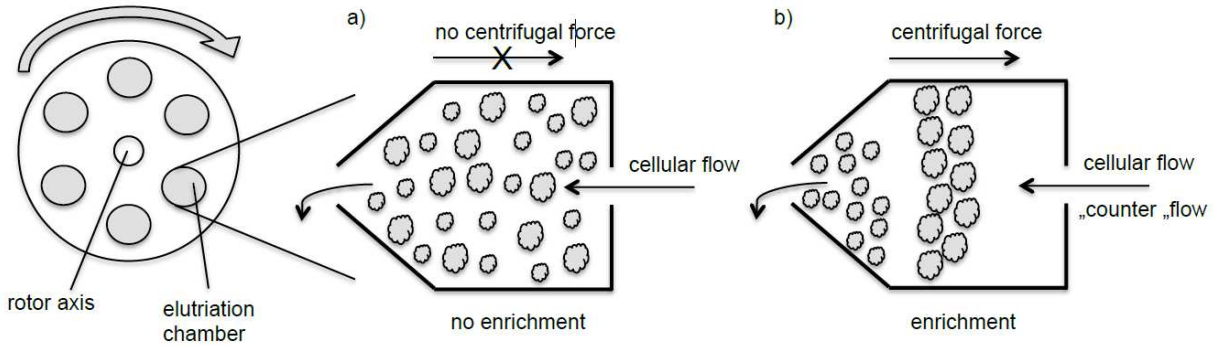

Ch IV S4 Figure 22 (2): Title needed *(talks about elutriation chambers)*

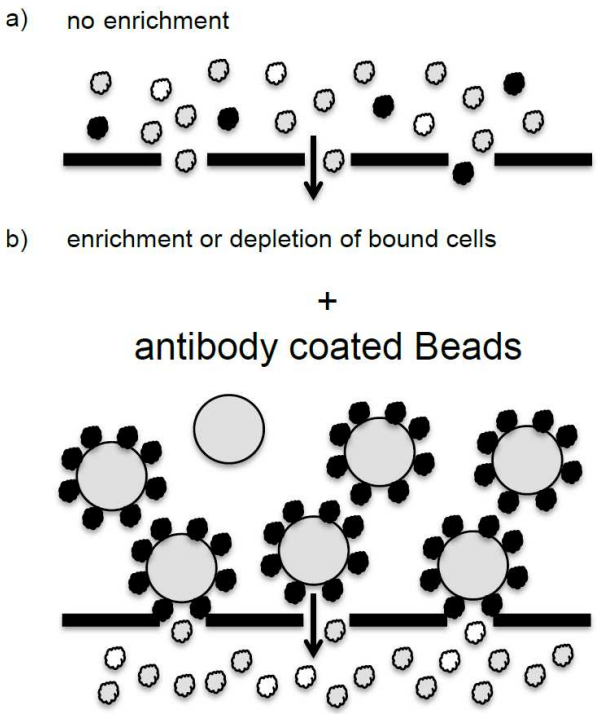

Ch IV S4 Figure 23 (3): Title needed *(talks about mesh size)*

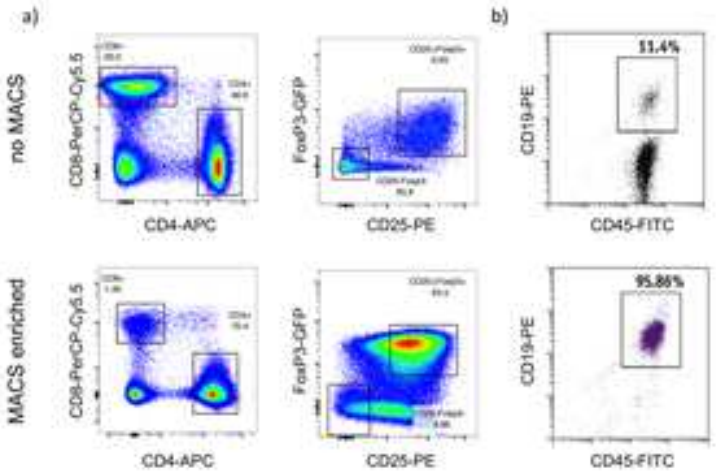

Ch IV S4 Figure 24 (4): Examples for MACS®-enriched cell populations.

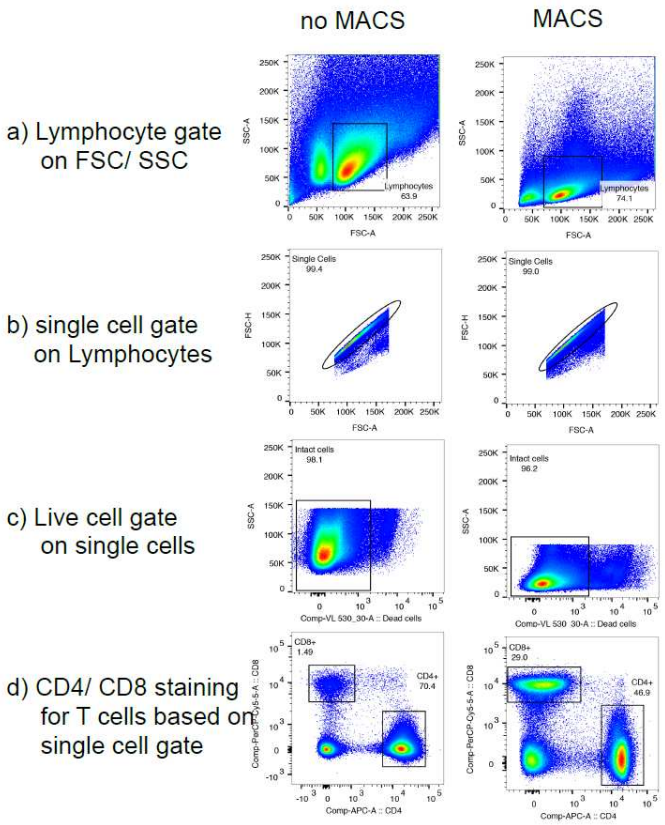

Ch IV S4 Figure 25 (5):Title needed *(talks about Tregs)*

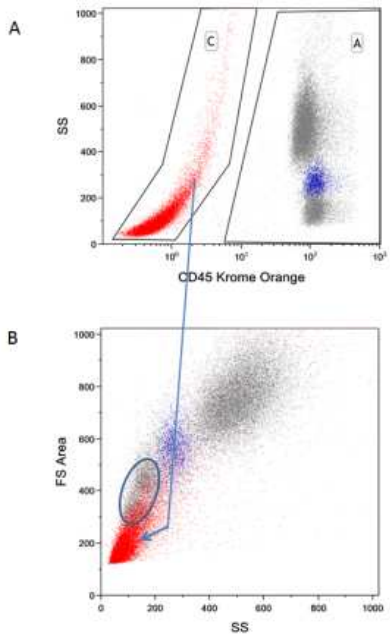

Ch IV S6 Figure 26 (1): Human whole blood fixed with formaldehyde and permeabilized with TX-100.

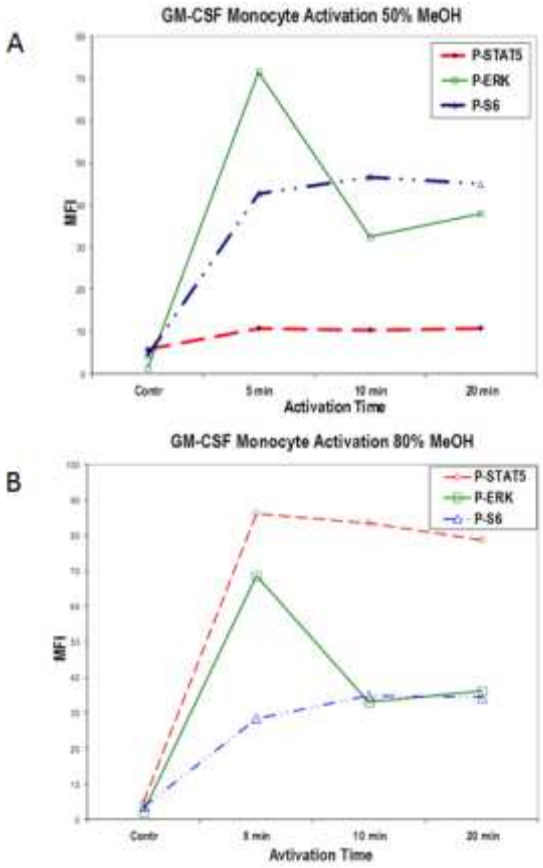

Ch IV S6 Figure 27 (2): Impact of methanol concentration on P-STAT5 immunoreactivity in peripheral blood monocytes activated in vitro using GM-CSF.

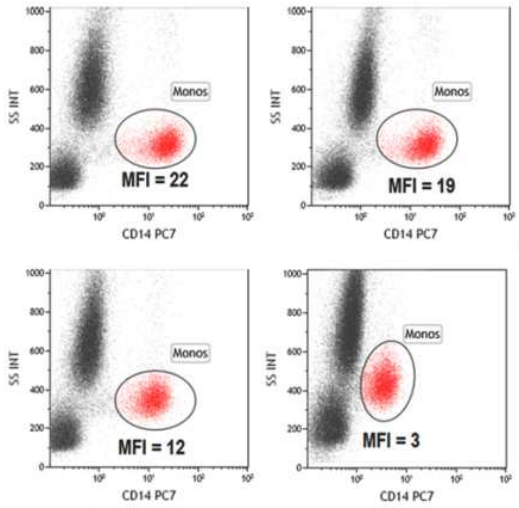

Ch IV S6 Figure 28 (3): Effect of methanol treatment on CD14 staining of human peripheral blood monocytes.

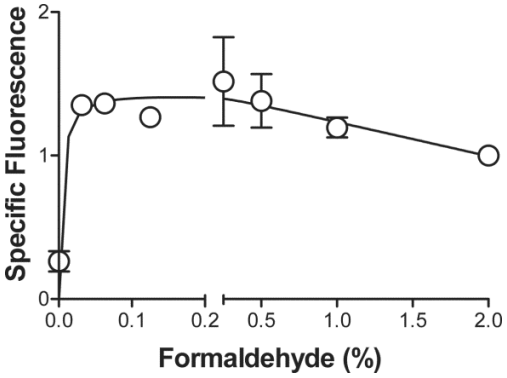

Ch IV S6 Figure 29 (4). Effect of formaldehyde concentration on P-STAT5 immunoreactivity in K562 cells (from reference 5, used with permission).

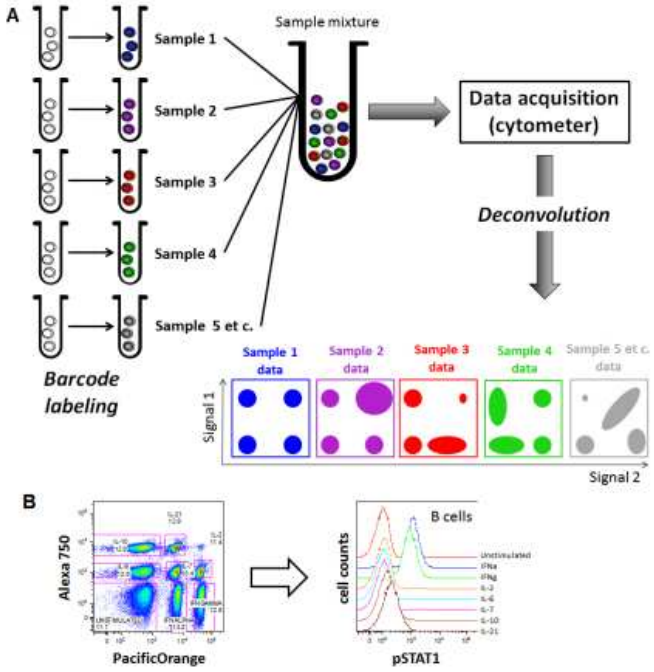

Ch IV S7 Figure 30 (1). Workflow of cell sample barcoding for flow and mass cytometry.

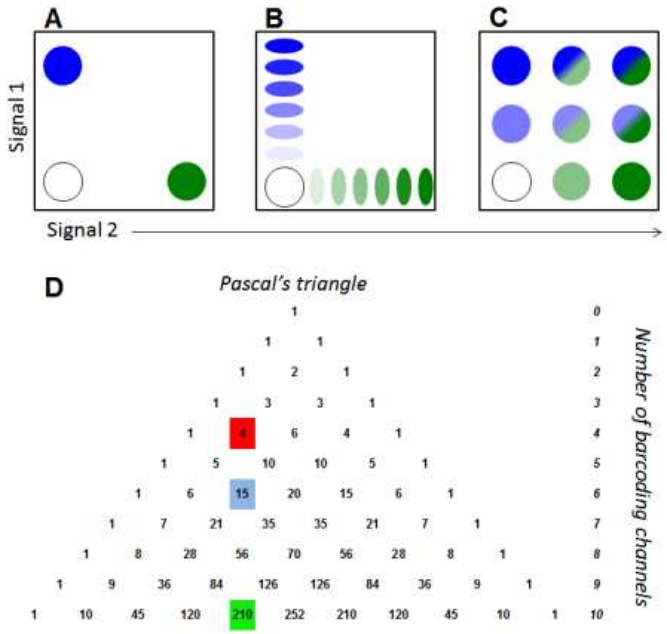

Ch IV S7 Figure 31 (2). Barcoding schemes.

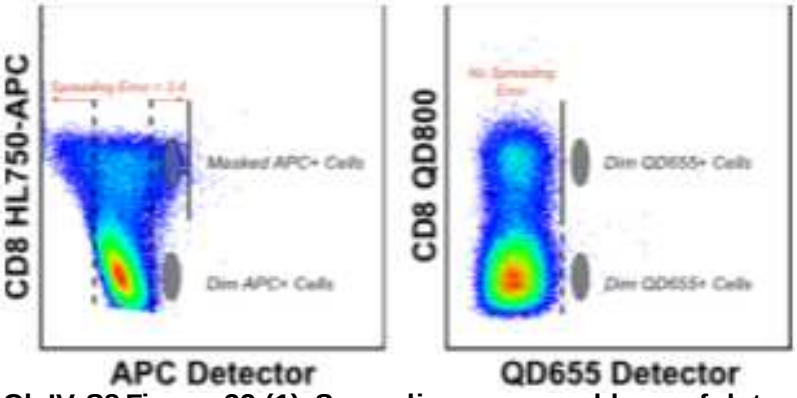

Ch IV S8 Figure 32 (1): Spreading error and loss of detection sensitivity.

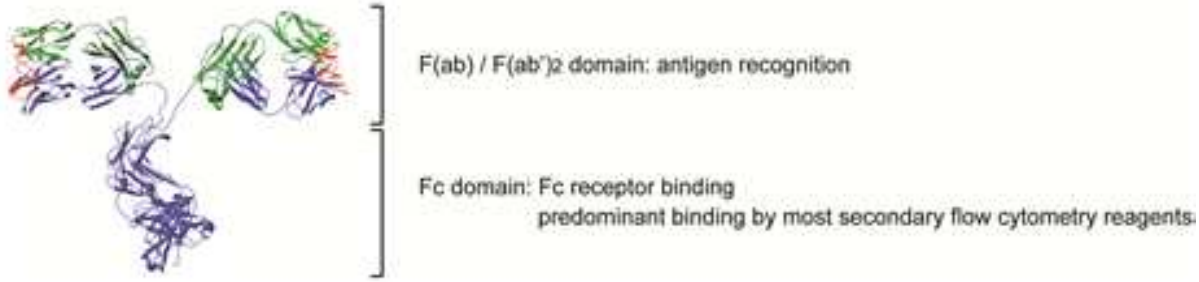

Ch IV S9 Figure 33 (1): Structural characteristics of immunoglobulins.

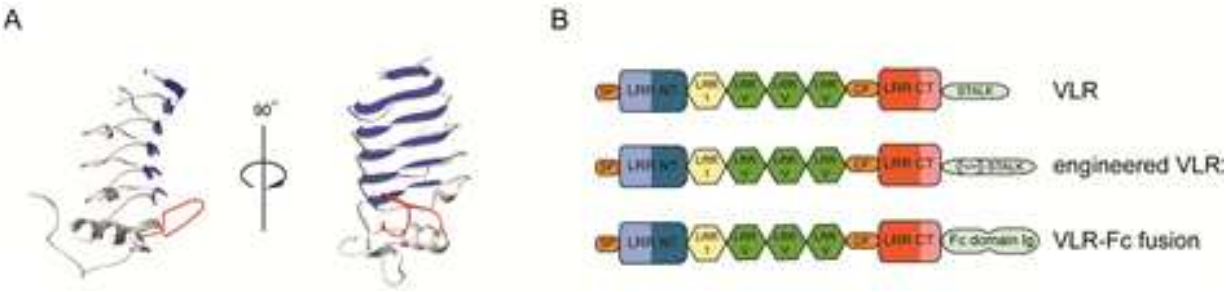

Ch IV S9 Figure 34 (2): Structural characteristics of VLR antibodies.

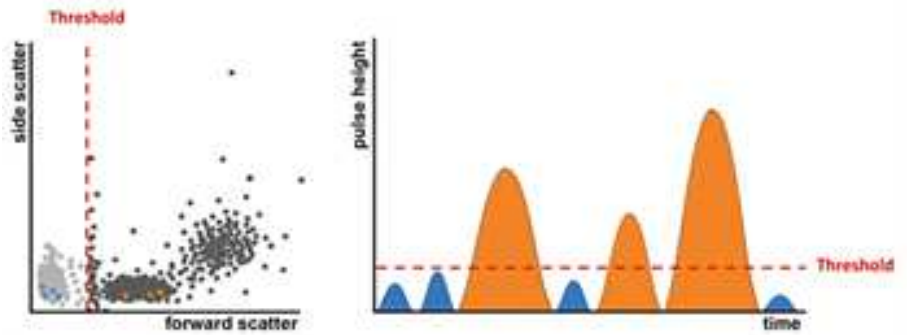

Ch V S2 Figure 35 (1): The threshold value defines a signal intensity, in one or more parameters, above which the cytometer starts to recognize an event. All other events will be invisible to the instrument's electronics.

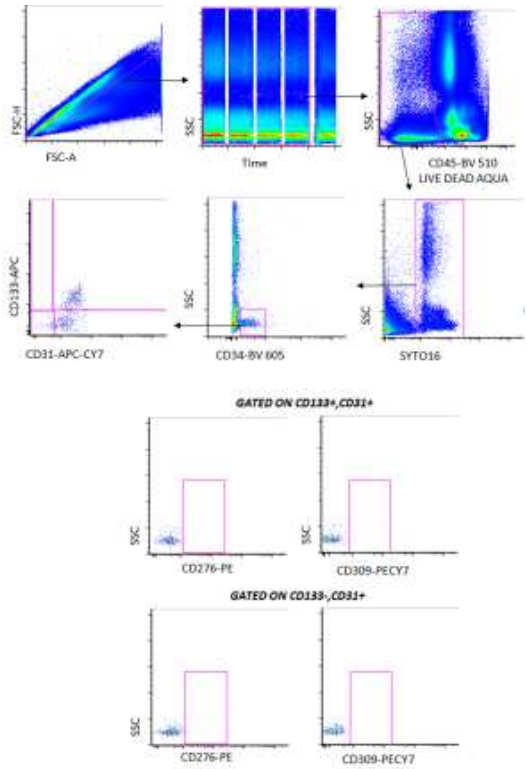

Ch V S3 Figure 36 (1). An example of a gating stategy for rare cells.

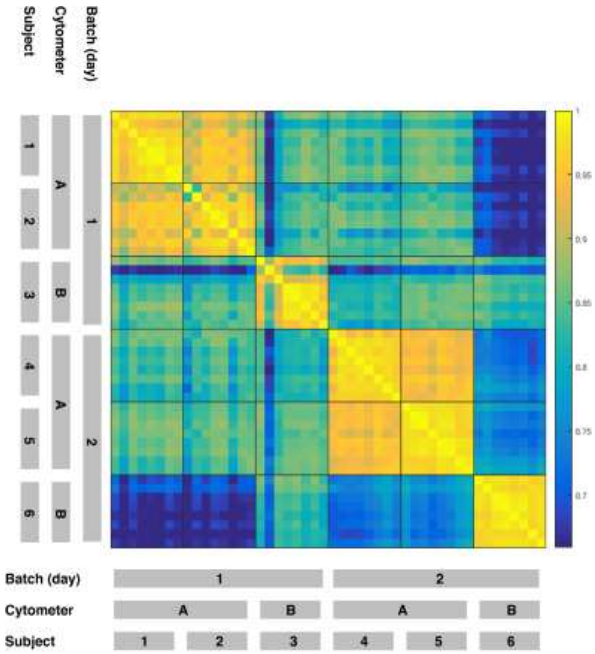

Ch VI S1 Figure 37 (1). Quality control analysis to detect batch effects.

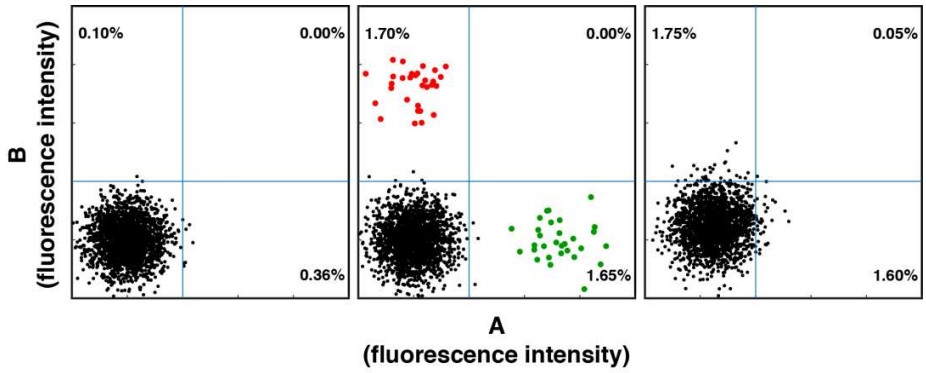

Ch VI S1 Figure 38 (2). Model data illustrating the very different interpretations of two samples with similar proportions of cells in a positive gate.

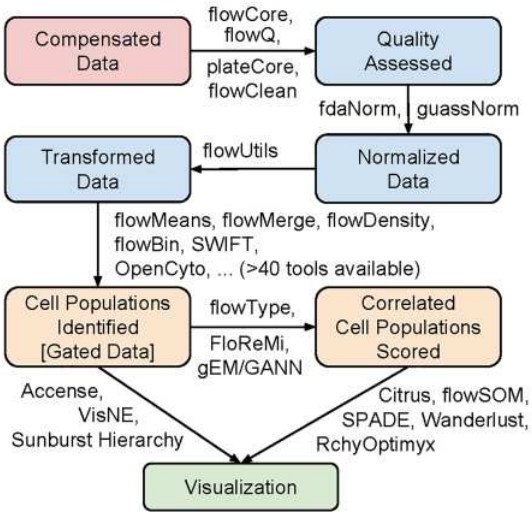

Ch VI S2 Figure 39 (1): Typical automated analysis workflows in flow cytometry.

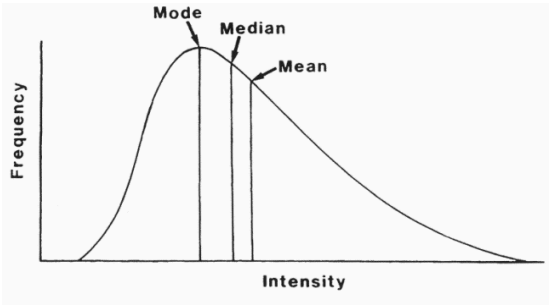

Ch VI S3 Figure 40 (1): Measurements of central tendencies for cytometric intensity histograms.

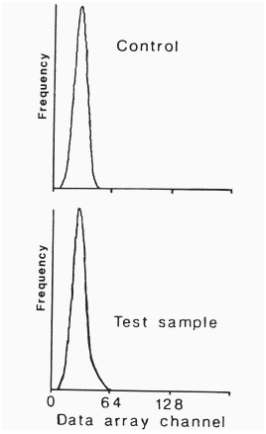

Ch VI S3 Figure 41 (2): The histogram representation of fluorescence from a weak staining of a small (rare) population.

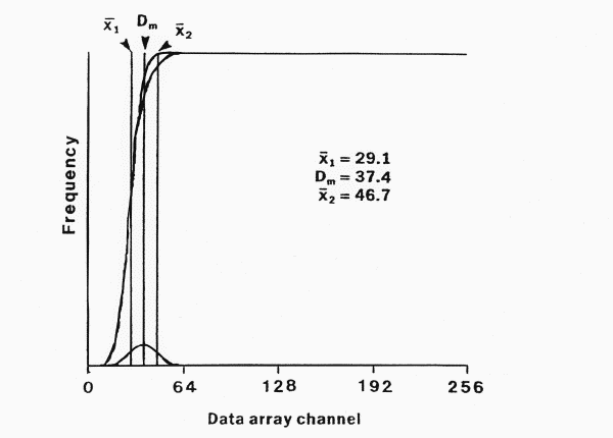

Ch VI S3 Figure 42 (3): Cumulative frequencies from the two histograms in Fig. 2 and difference.

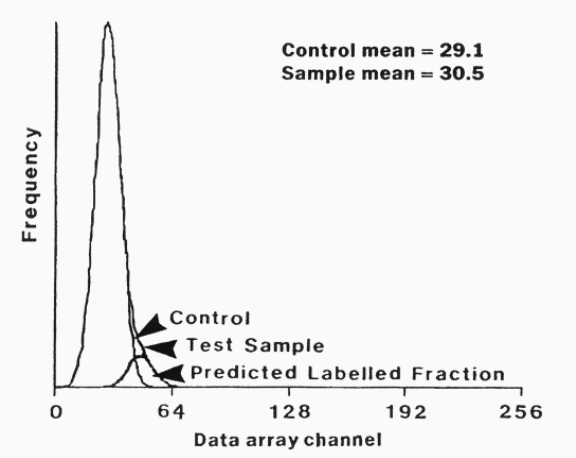

Ch VI S3 Figure 43 (4): Result of the histogram analysis.

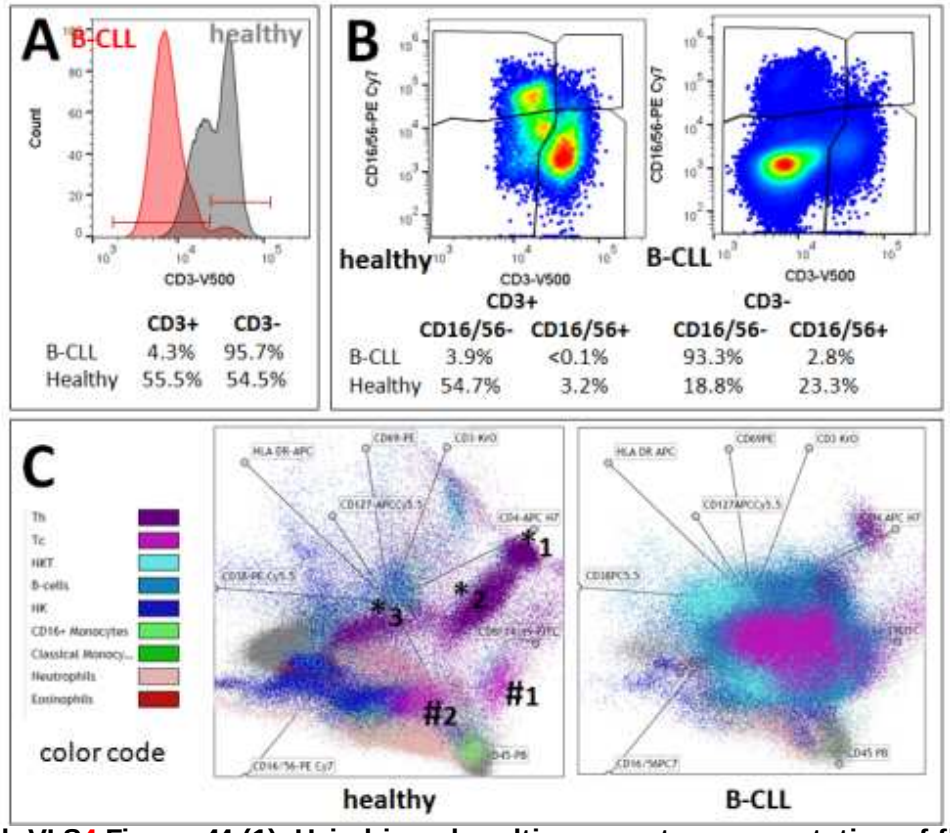

Ch VI S4 Figure 44 (1). Uni-, bi- and multi-parameter presentation of flow data.

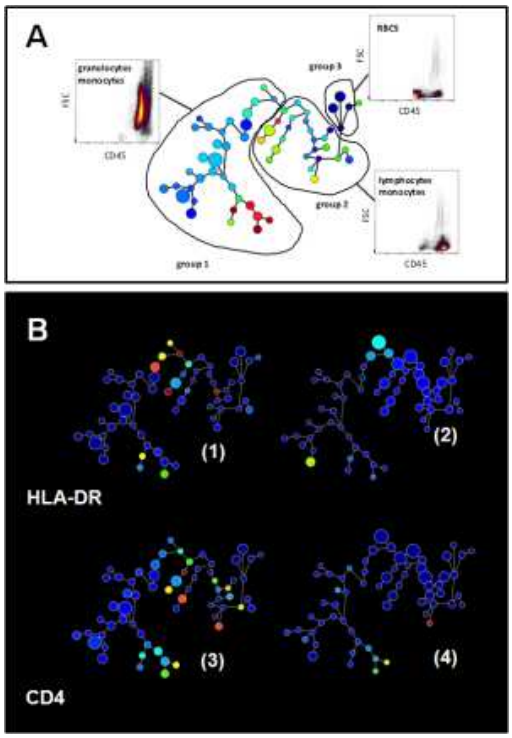

Ch VI S4 Figure 45 (2). Semi-automated analysis of flow cytometric data by SPADE.

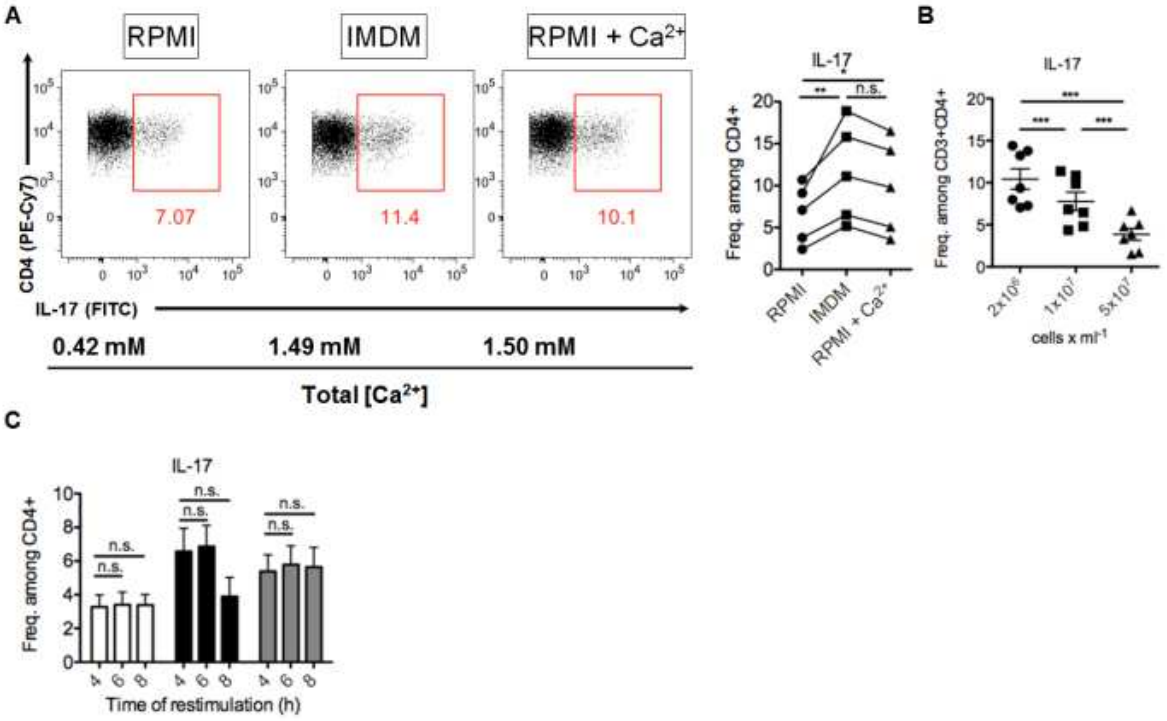

Ch VII S3 Figure 46 (1). An example of intracellular cytokine detection.

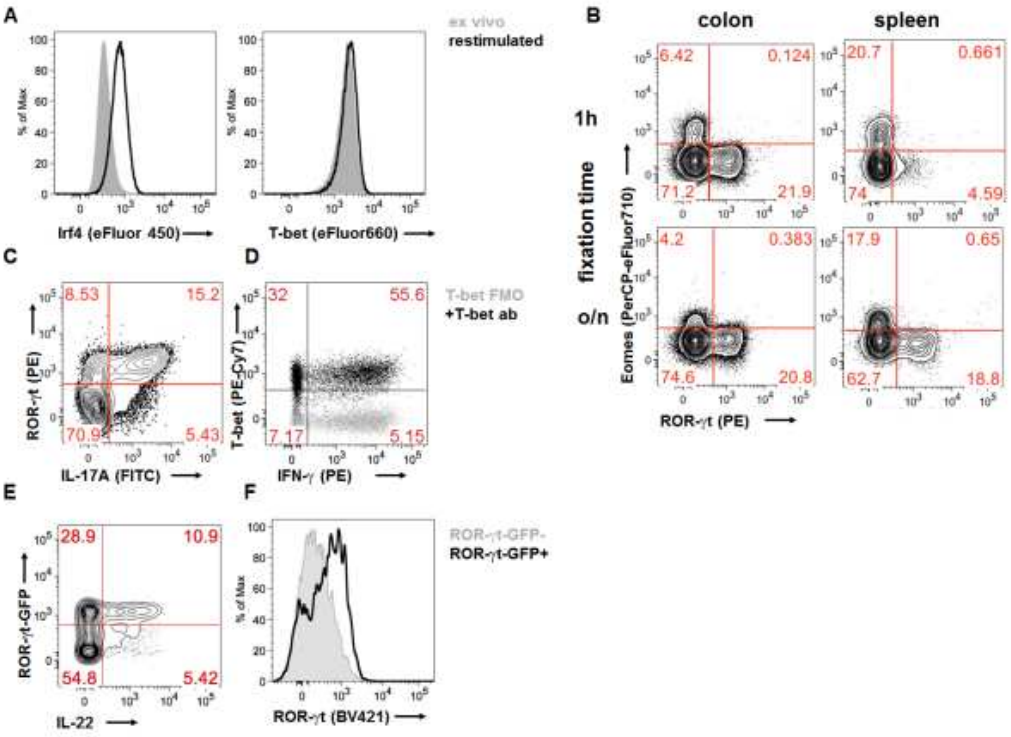

Ch VII S3 Figure 47 (2). An example of intranuclear transcription factor detection.

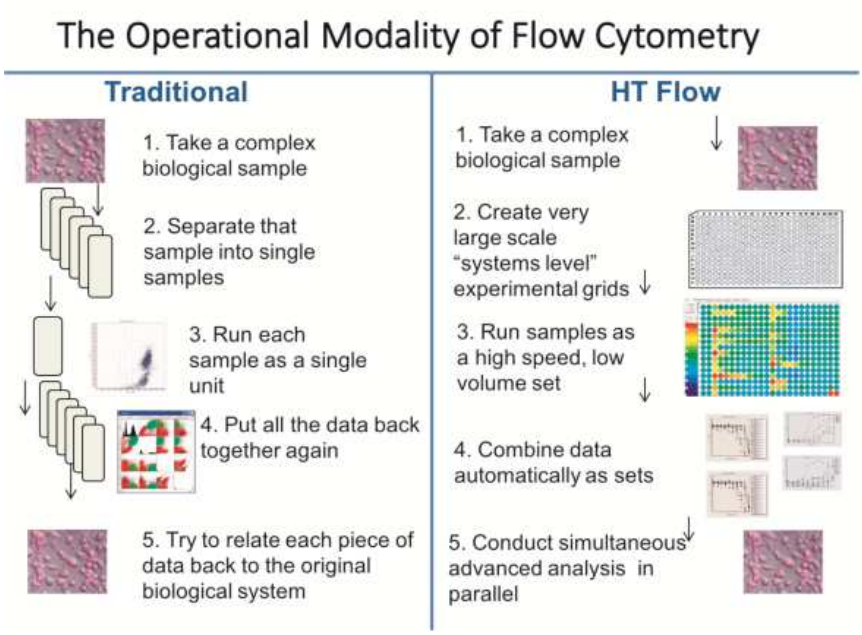

Ch VII S4 Figure 48 (1): An example of how a traditional flow cytometry assay might be designed using test tubes or even a 96 well plate assay.

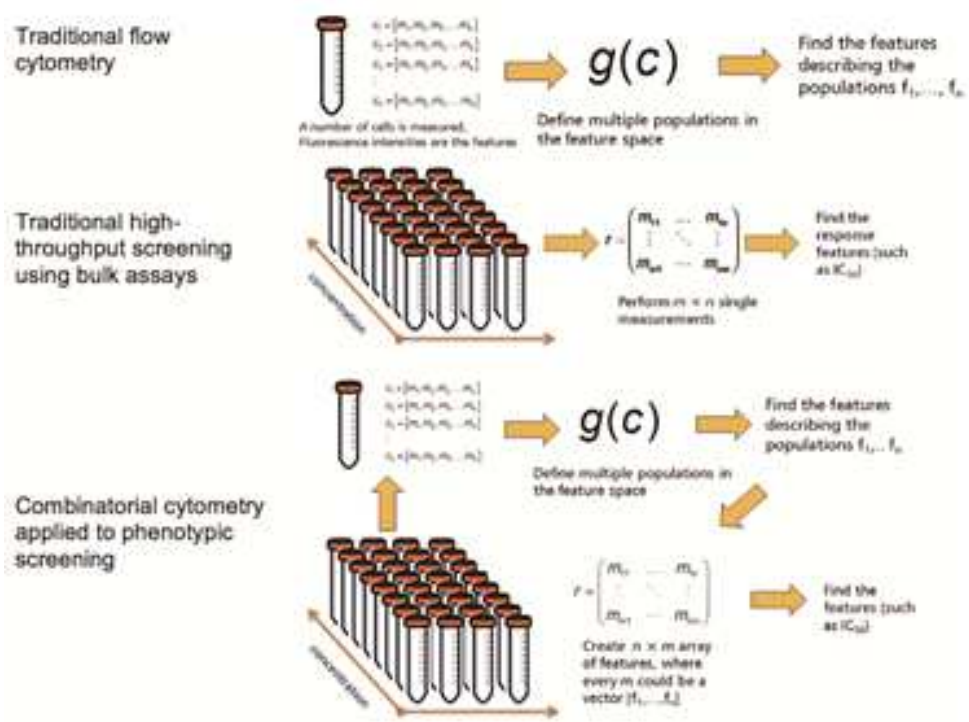

Ch VII S4 Figure 49 (2): Combinatorial cytometry integrates the ideas of screening biological responses.

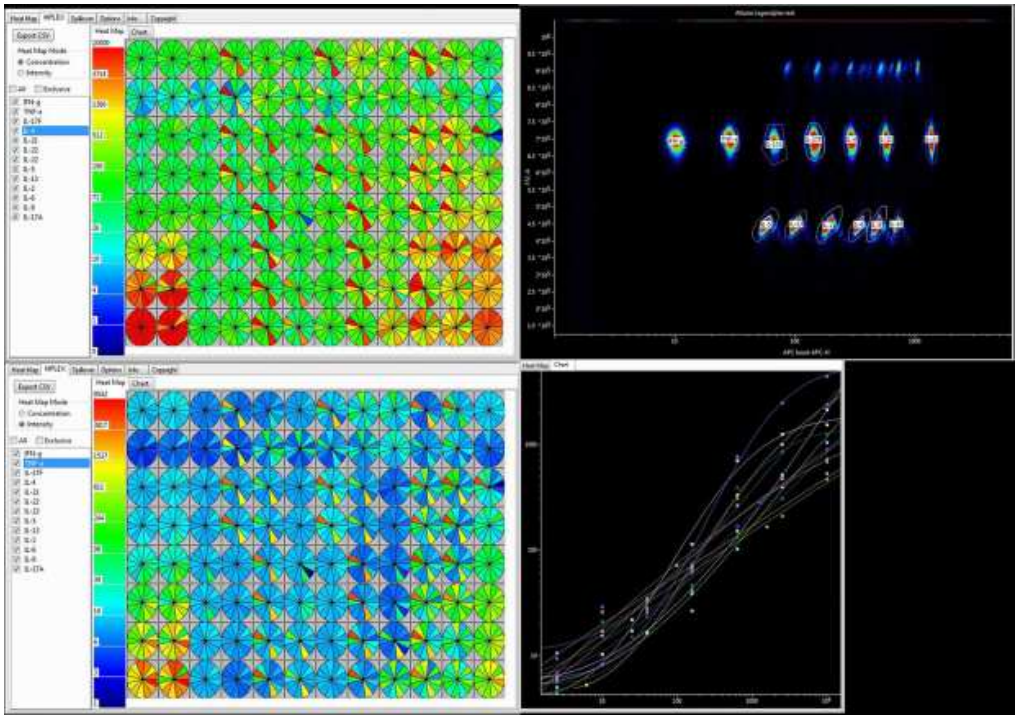

Ch VII S4 Figure 50 (3): Automated processing of bead-based cytokine assay.

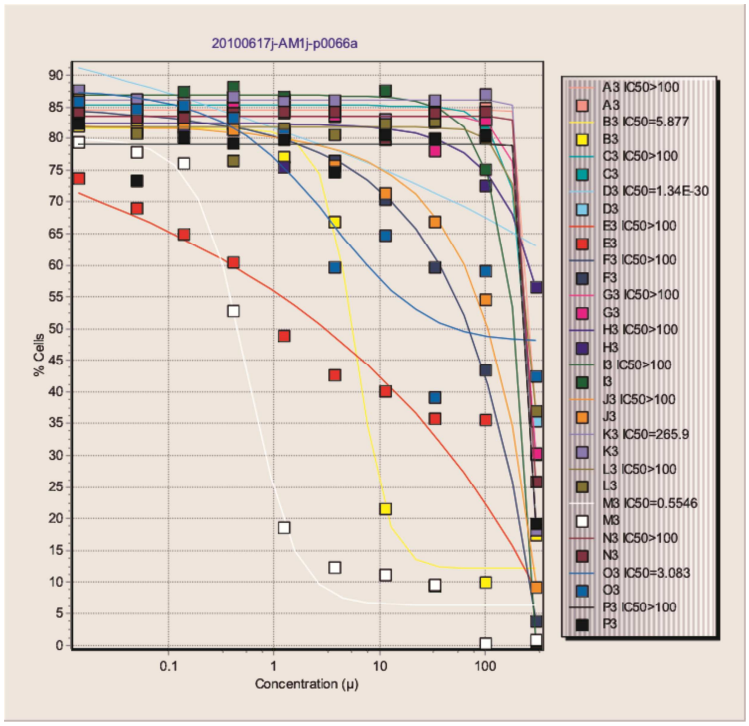

Ch VII S4 Figure 51 (4): Response curves automatically produced from data extracted from multiple FCS files.

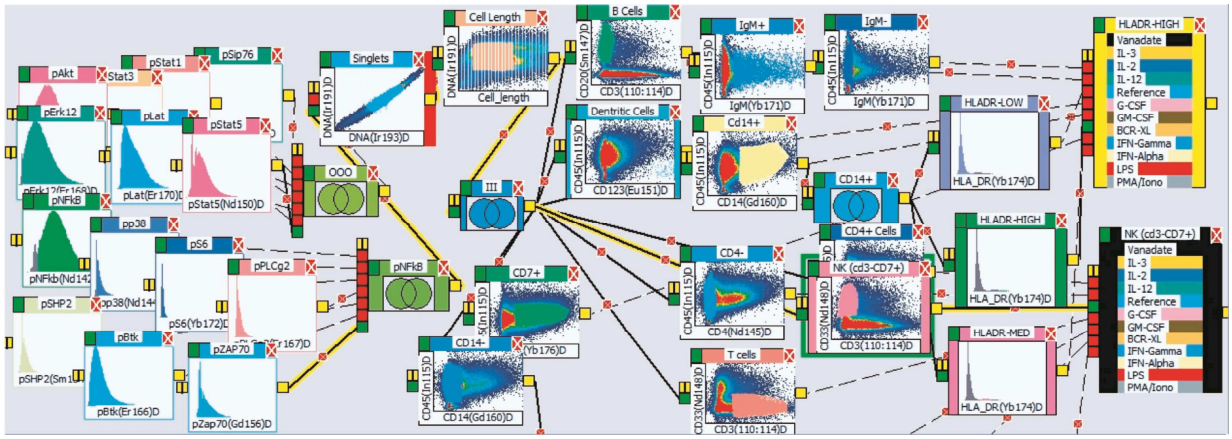

Ch VII S4 Figure 52 (5): The pipeline design canvas of the Plate Analyzer.

PE	APC	Qdot605	Qdot625	Qdot655	Qdot705	Qdot800	PE-Cy7	
	Peptide 1	Peptide 2	Peptide 3	Peptide 4	Peptide 5	Peptide 6	Peptide 7	PE
		Peptide 8	Peptide 9	Peptide10	Peptide11	Peptide12	Peptide13	APC
			Peptide14	Peptide15	Peptide16	Peptide17	Peptide18	Qdot605
				Peptide19	Peptide20	Peptide21	Peptide22	Qdot625
					Peptide23	Peptide24	Peptide25	Qdot655
						Peptide26	Peptide27	Qdot705
							Peptide28	Qdot800
								PE-Cy7

PE	APC	Qdot605	Qdot625	Qdot655	Qdot705	Qdot800	PE-Cy7	
	Peptide 1	Peptide 2	Peptide 3	Peptide 4	Peptide 5	Peptide 6	Peptide 7	PE
		Peptide 8	Peptide 9	Peptide10	Peptide11	Peptide12	Peptide13	APC
			Peptide14	Peptide15	Peptide16	Peptide17	Peptide18	Qdot605
				Peptide19	Peptide20	Peptide21	Peptide22	Qdot625
					Peptide23	Peptide24	Peptide25	Qdot655
						Peptide26	Peptide27	Qdot705
							Peptide28	Qdot800
								PE-Cy7

Ch VII S5 Figure 53 (1): An example of a combinatorial staircase giving 28 unique dual color codes to 28 different peptides.

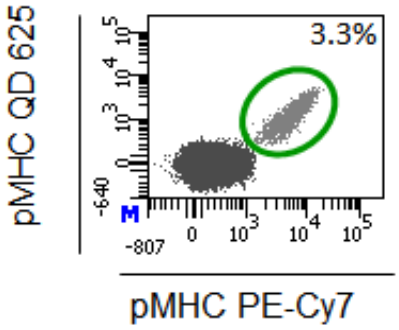

Ch VII S5 Figure 54 (2): Dot plots showing an antigen specific T cell population detected in T cells isolated from a tumor lesion.

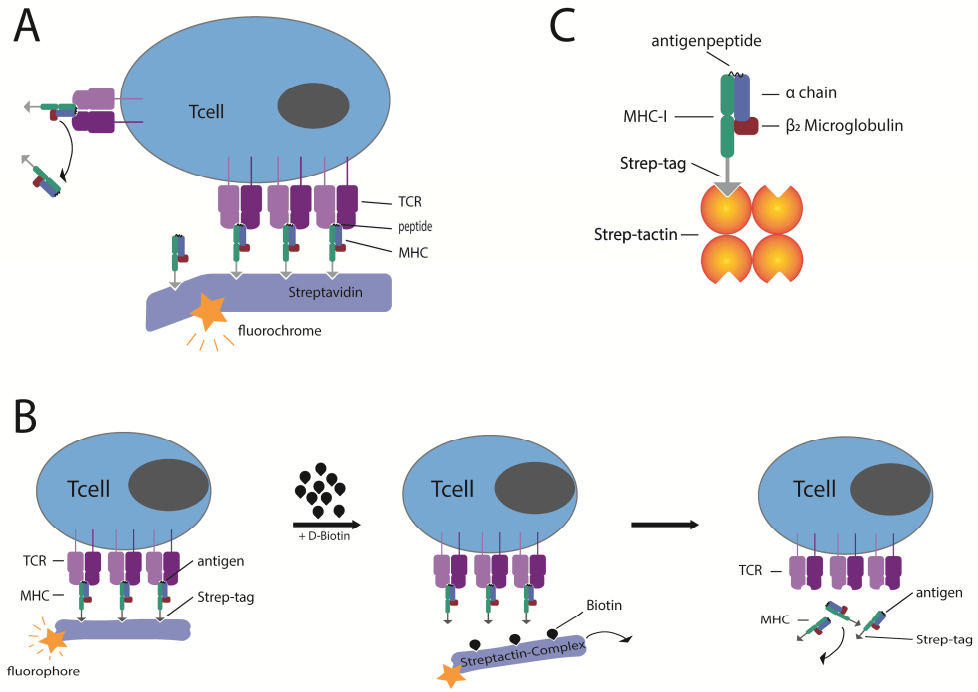

Ch VII S6.1 Figure 55 (1): Principle of MHC multimer staining by increasing the binding avidity of MHC-TCR interactions.

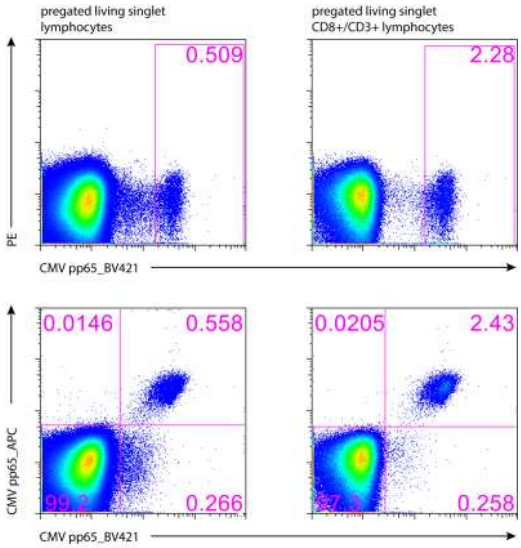

Ch VII S6.1 Figure 56 (2): MHC multimer staining of human PBMCs for CMV peptide pp65 with BV421 and APC.

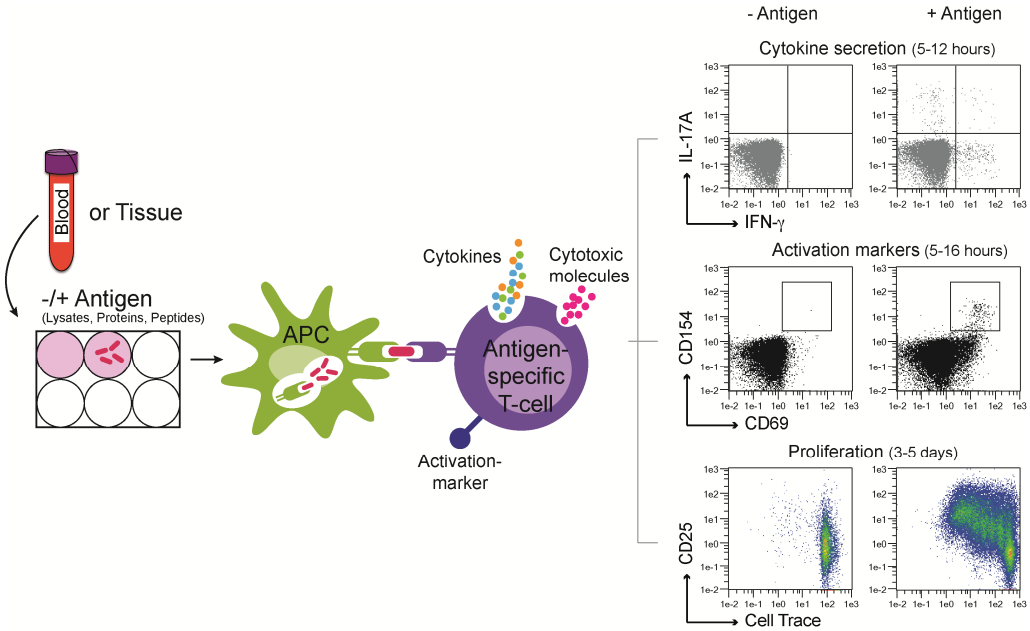

Ch VII S6.2 Figure 57 (1). Principle of antigen-specific stimulation assays.

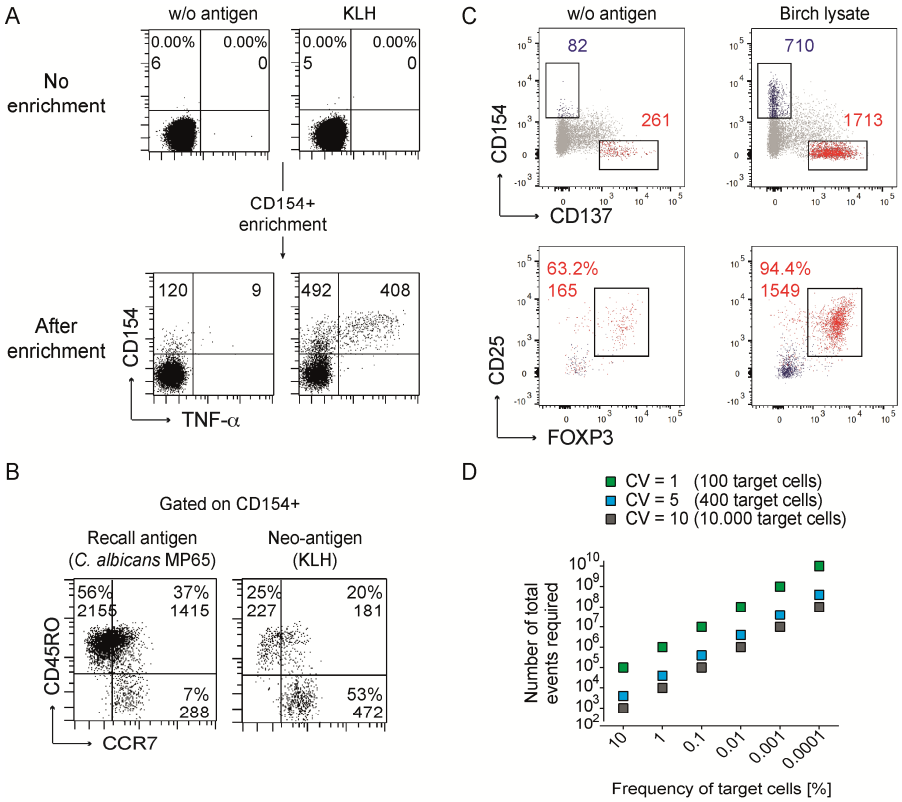

Ch VII S6.2 Figure 58 (2). Enrichment of antigen-specific T cells increases sensitivity for the detection of rare cells.

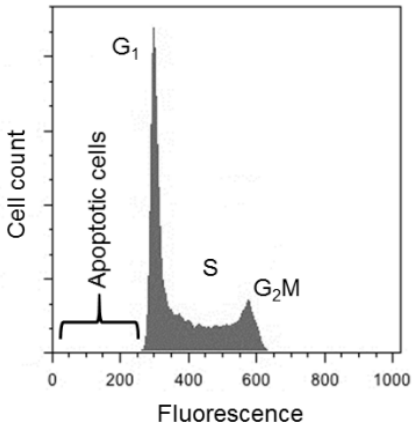

Ch VII S7 Figure 59 (7.1). Representative DNA fluorescence histogram of PI-stained cells.

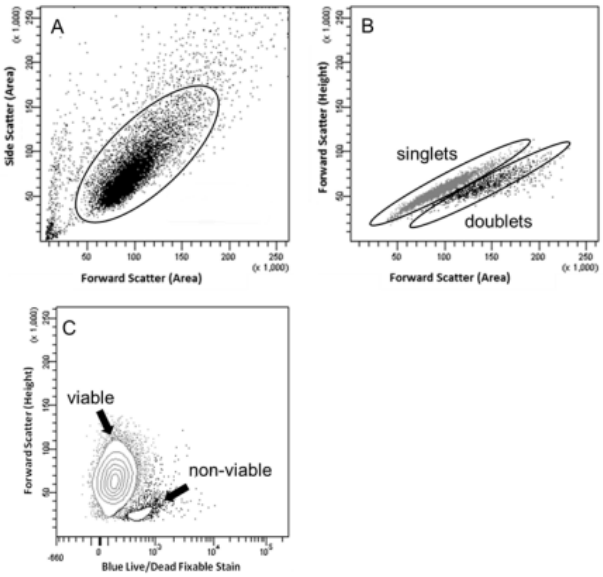

Ch VII S7 Figure 60 (7.2): Identification of single cell populations for analysis using flow cytometry.

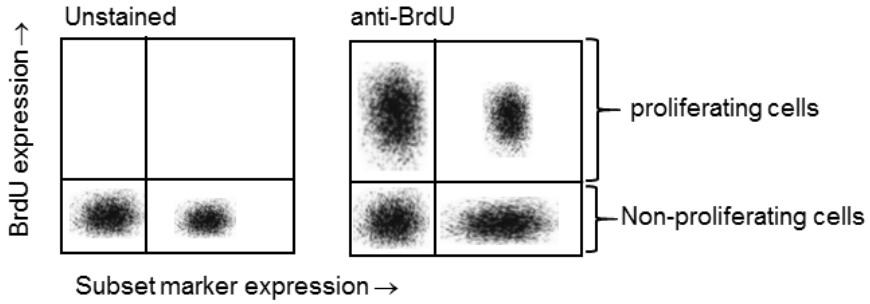

Ch VII S7 Figure 61 (7.3): Schematic representation of fluorescent dot plot for the flow cytometric analysis of cell proliferation on the basis of BrDU incorporation.

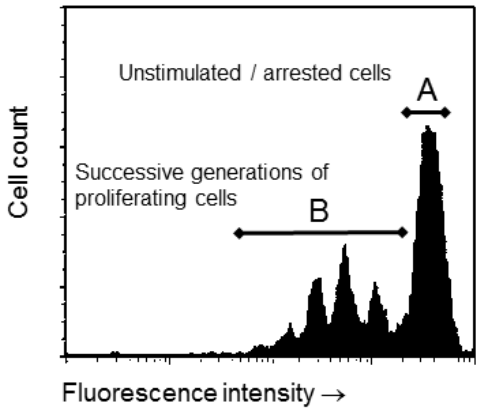

Ch VII S7 Figure 62 (7.4): Schematic fluorescence histogram depicting a progressive decline in the fluorescent intensity of proliferating cells stained with CFSE.

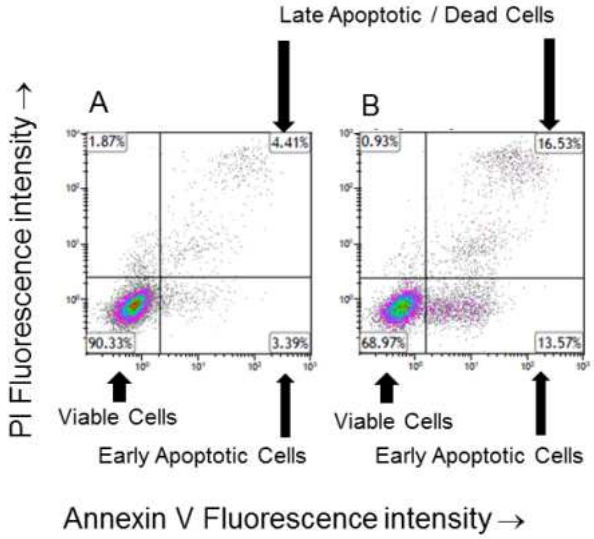

Ch VII S8.4 Figure 63 (1): Identifying healthy and apoptotic cells on the basis of Annexin V staining.

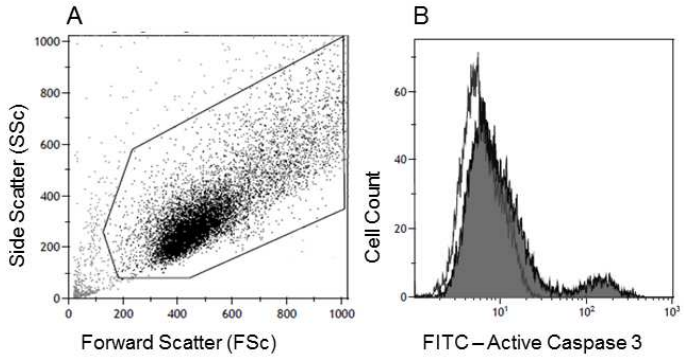

Ch VII S8.5 Figure 64 (1): Identifying healthy and apoptotic cells on the basis of activated caspase-3 expression.

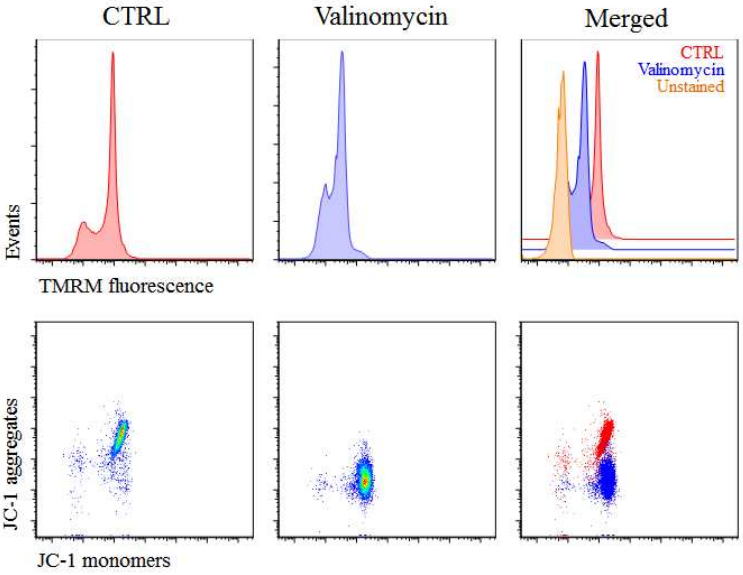

Ch VII S8.6 Figure 65 (1). TMRM and JC-1 staining of $CD4^+$ T cells.

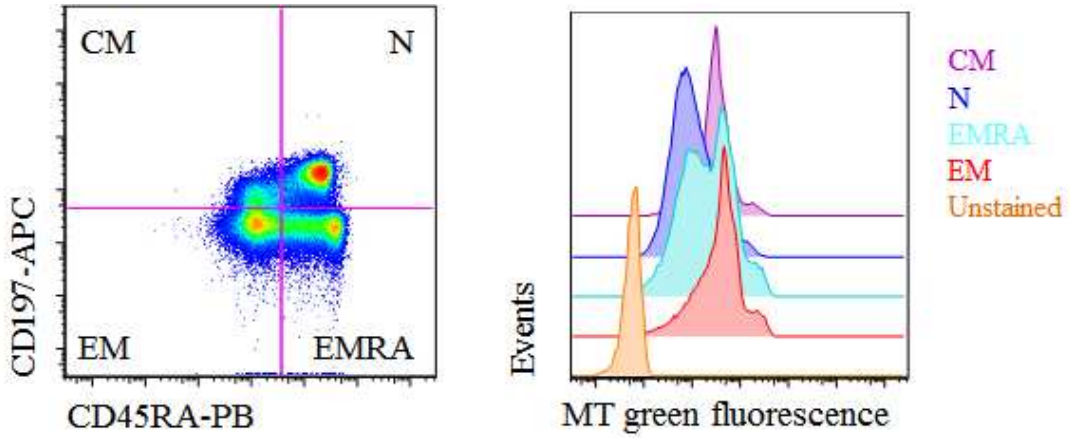

Ch VII S8.6 Figure 66 (2): Mitotracker Green staining of different subsets of CD8$^+$ T cells.

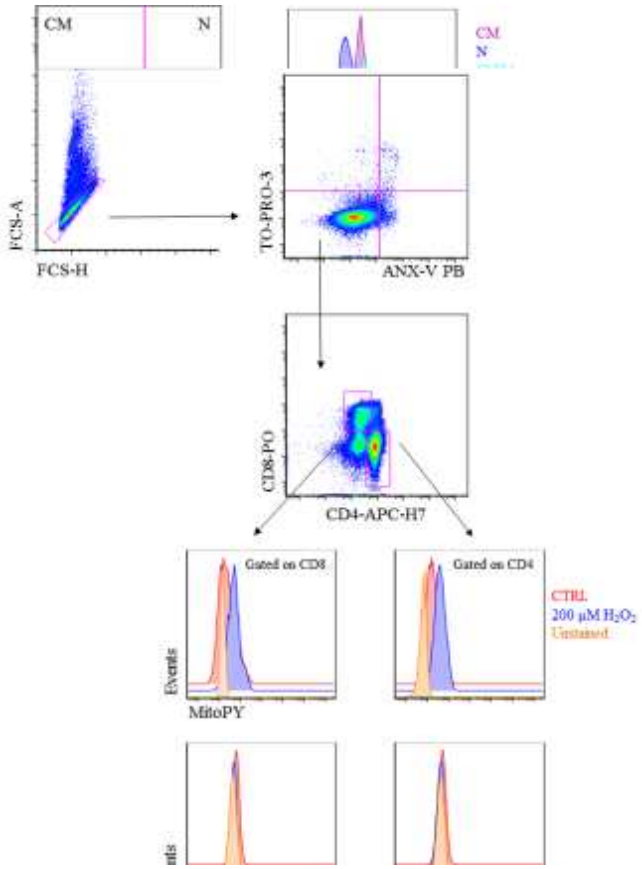

Ch VII S8.6 Figure 67 (3): MitoSOX Mitochondrial Red superoxide indicator and Mitochondria Peroxy Yellow-1 staining of different subsets of CD8$^+$ T cells.

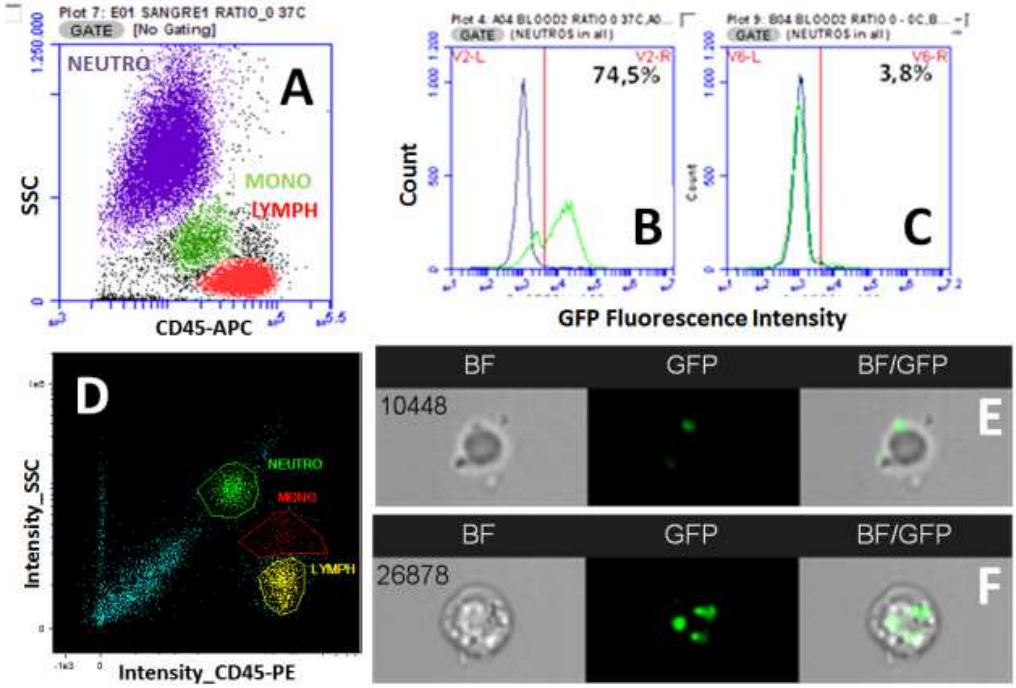

Ch VII S9 Figure 68 (1): Representative examples of strategies to differentiate between attached and internalized fluorescent bacteria in whole-blood phagocytosis assays by conventional flow cytometry (A–C) and imaging flow cytometry (D–F).

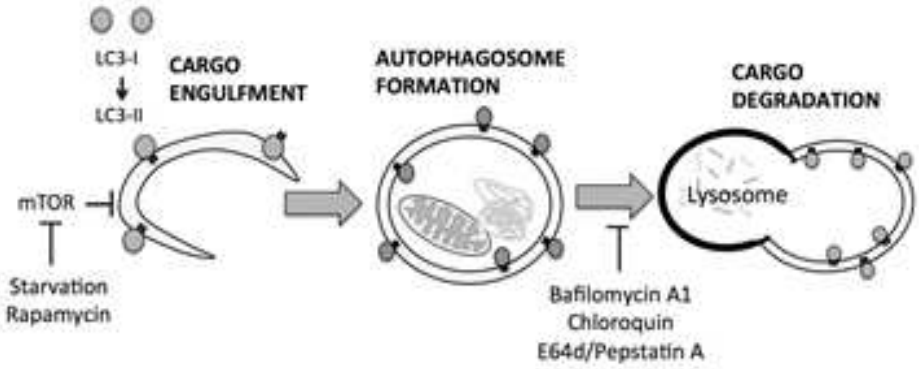

Ch VII S10 Figure 69 (1): Autophagy pathway showing key modulators used in detection of autophagy.

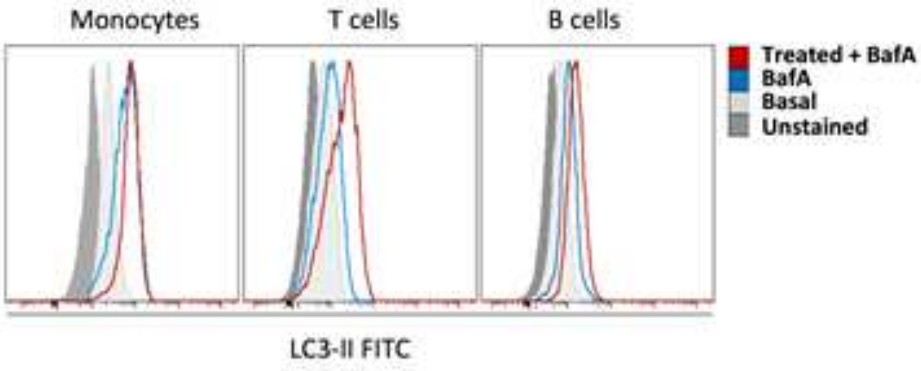

Ch VII S10 Figure 70 (2): Autophagy induction and flux measured with the FlowCellect LC3 kit.

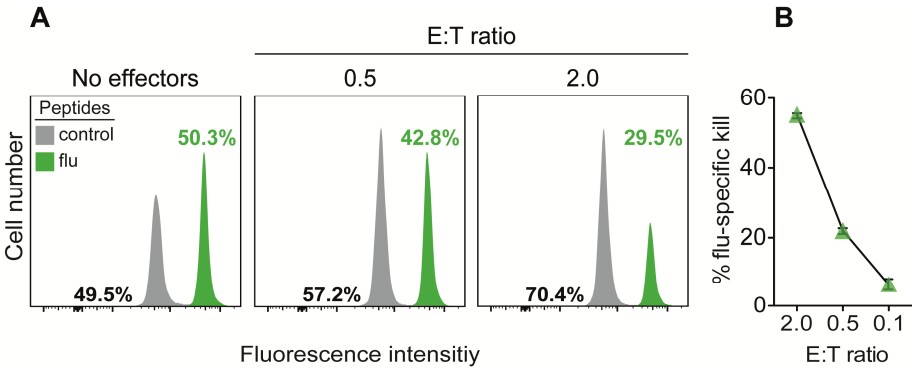

Ch VII S11 Figure 71 (1): Quantification of *ex vivo* cytotoxicity by influenza-specific CTLs.

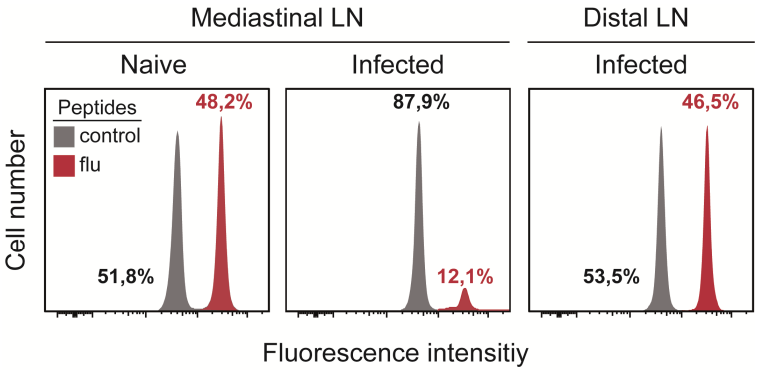

Ch VII S11 Figure 72 (2): Quantification of *in vivo* cytotoxicity by influenza-specific CTLs.

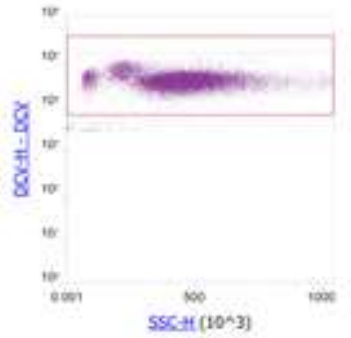

Ch VII S12 Figure 73 (1): Identification of leukocytes in human whole blood using violet laser and Vybrant DyeCycle Violet stain on the Attune NxT Flow Cytometer.

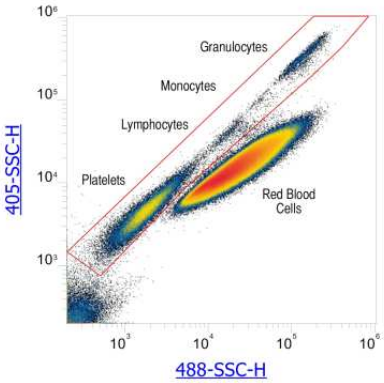

Ch VII S12 Figure 74 (2): Identification of leukocytes in human whole blood using violet side scatter on the flow cytometer.

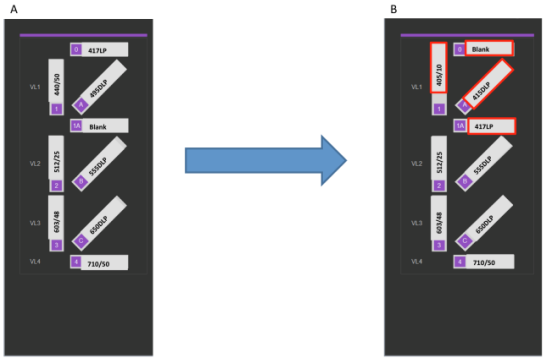

Ch VII S12 Figure 75 (3): Use of the Attune NxT No-Wash No-Lyse Filter Kit.

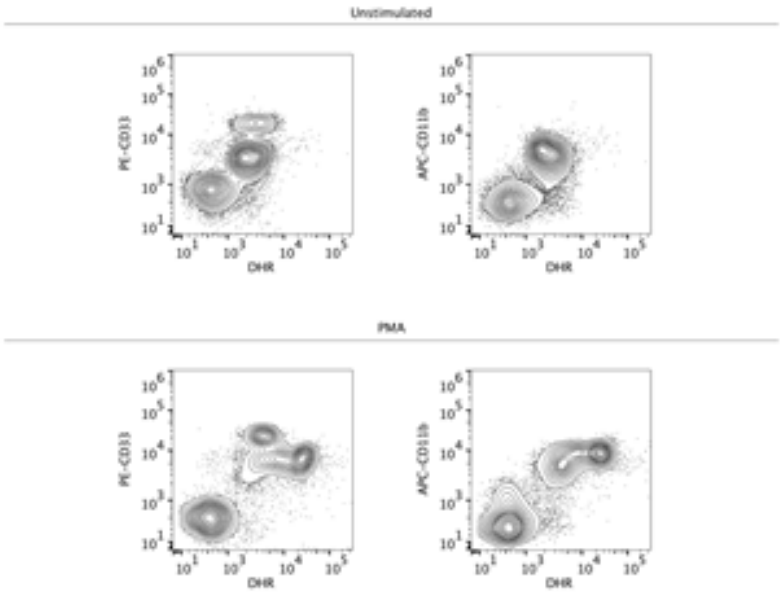

Ch VII S12 Figure 76 (4): Reactive oxygen species production.

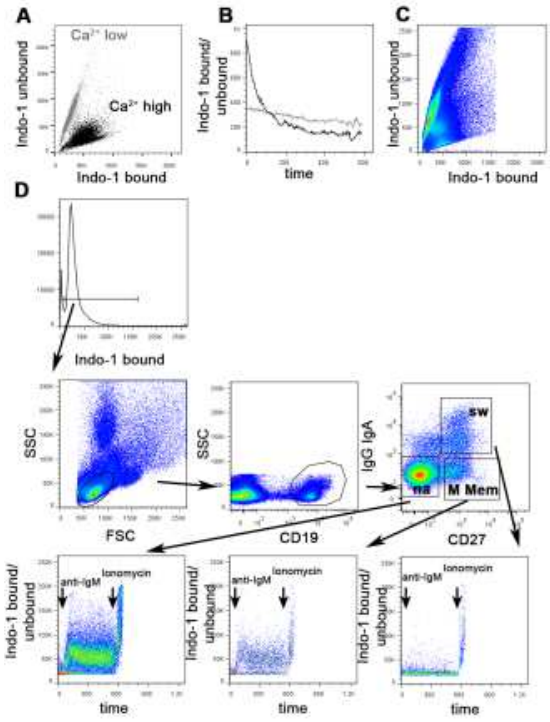

Ch VII S13 Figure 77 (1): Measuring intracellular Ca^{2+} mobilization in human B cells in response to anti-IgM stimulation after labeling with Indo-1 AM by flow cytometry.

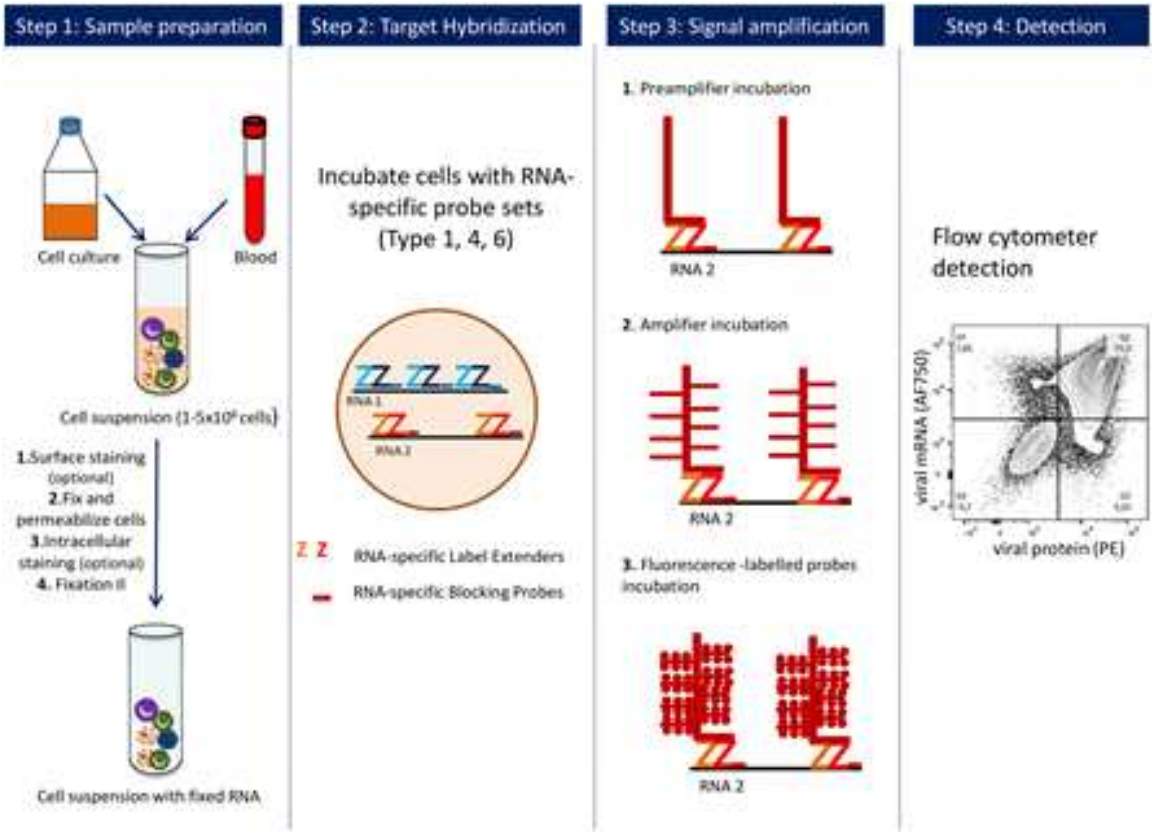

Ch VII S14 Figure 78 (1): PrimeFlow™ RNA Assay procedure

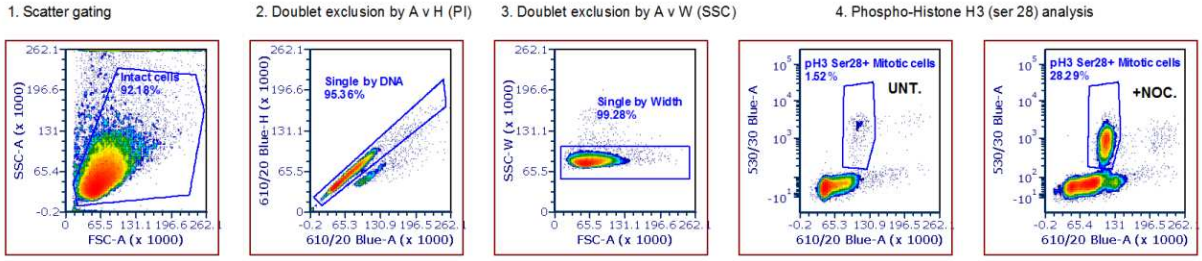

Ch VII S15 Figure 79 (1): Typical sequential gating analysis performed on samples of cycling cells stained for DNA content and intra-nuclear histone modifications.

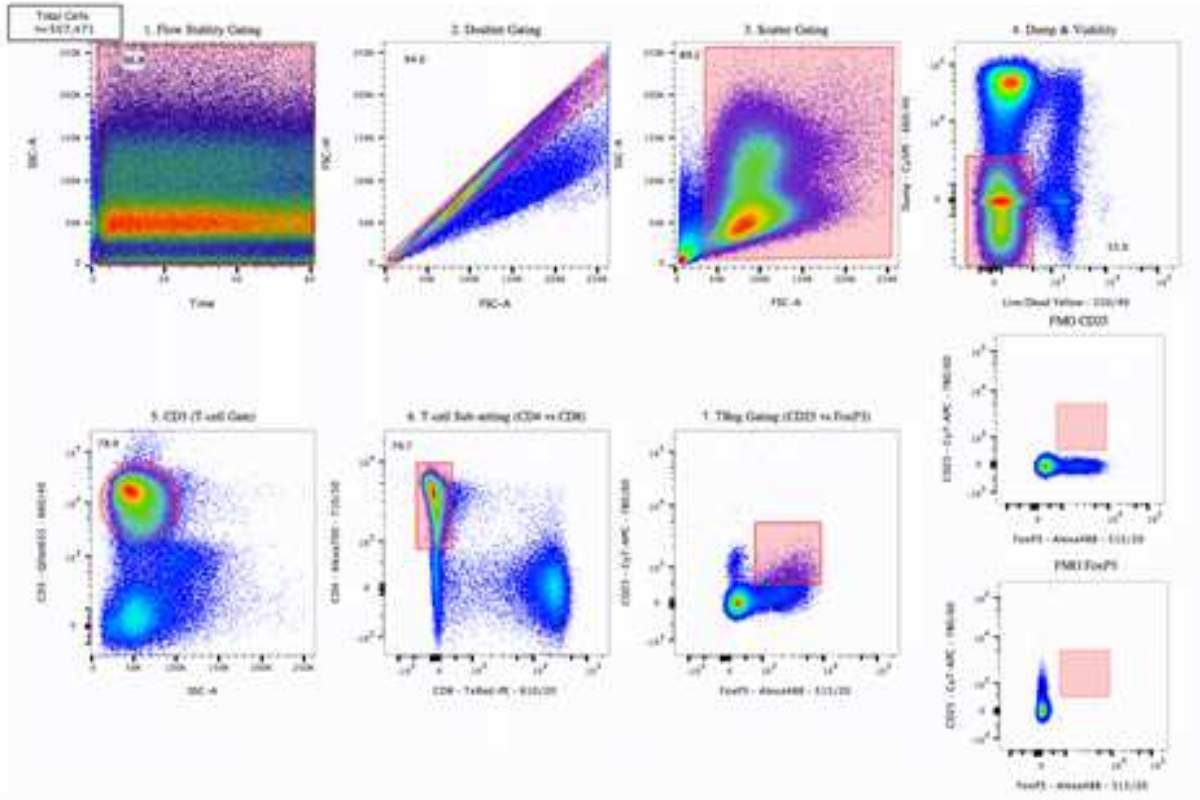

Ch VII S15 Figure 80 (2). FoxP3 staining to detect T-regulatory cells.

Figure 1

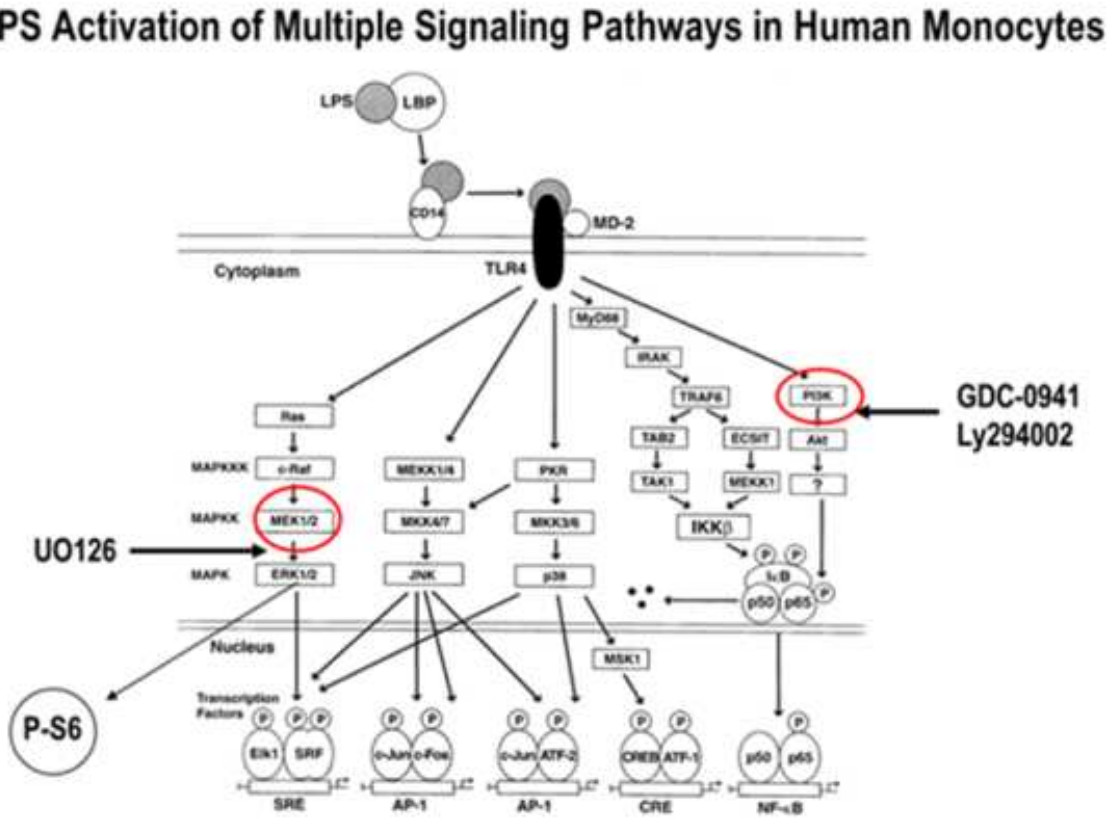

Ch VII S16 Figure 81 (1): "Canonical" pathways for LPS activation of multiple signaling pathways in peripheral blood monocytes via TLR-4 (adapted from Guha and Mackman, 2001).

Figure 2

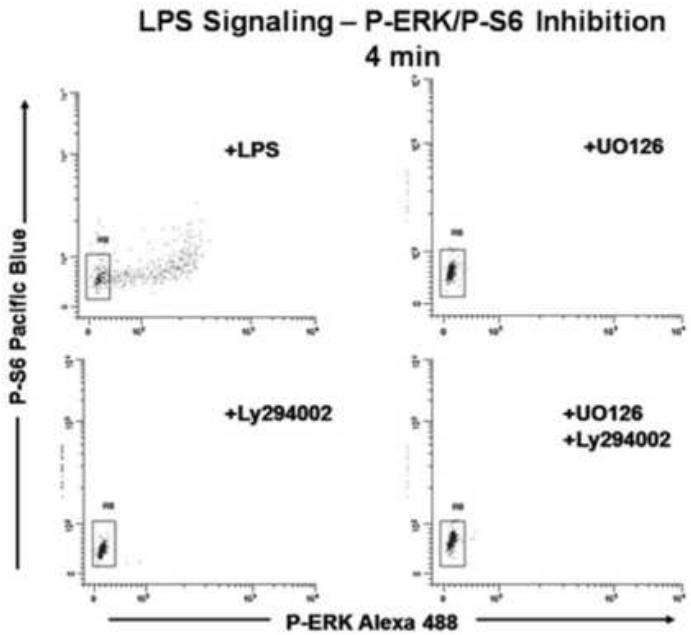

Ch VII S16 Figure 82 (2): LPS activation of the ERK pathway in human peripheral blood monocytes.

Figure 3

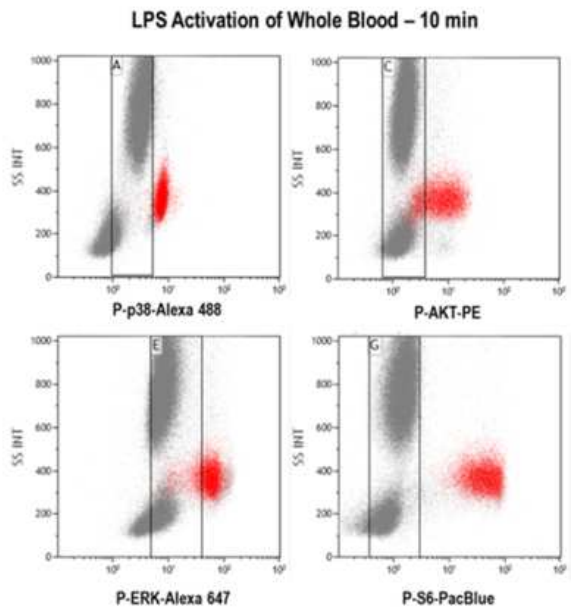

Ch VII S16 Figure 83 (3): Simultaneous measurement of four different signaling targets.

Figure 4

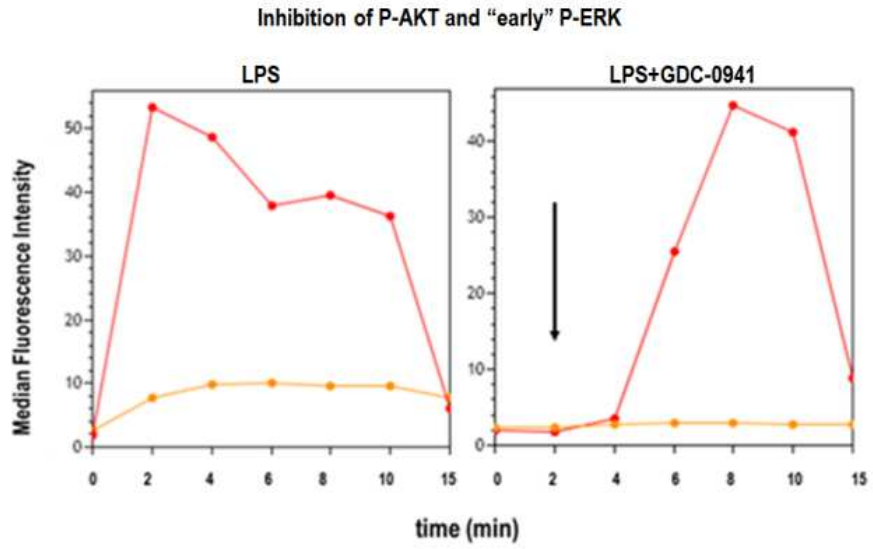

Ch VII S16 Figure 84 (4): Kinetics of LPS activation of the AKT and ERK pathways in peripheral blood monocytes.

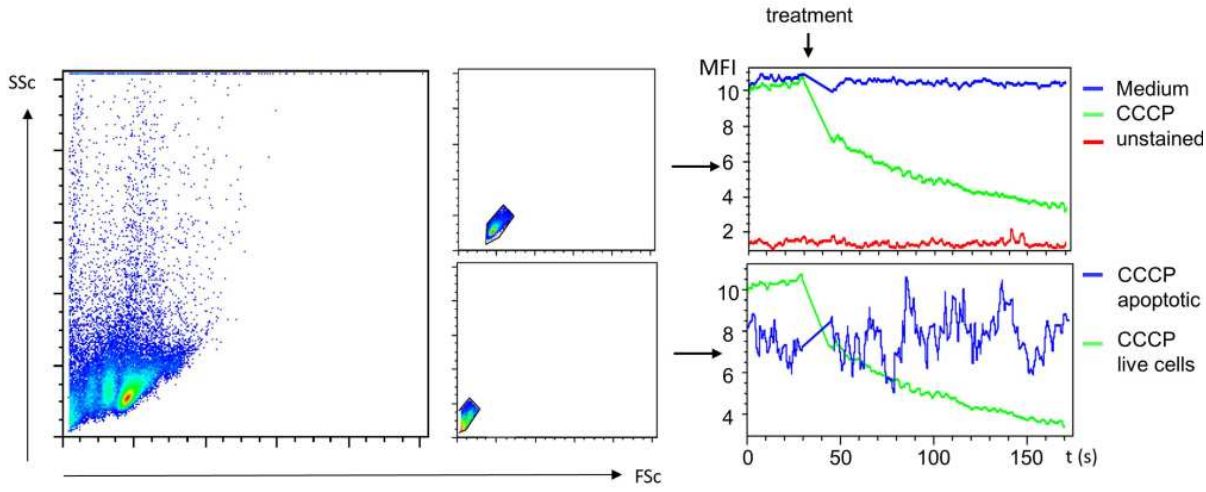

Ch VII S17 Figure 85 (1): Analysis of the sensitivity of mtmP towards CCCP in real time.

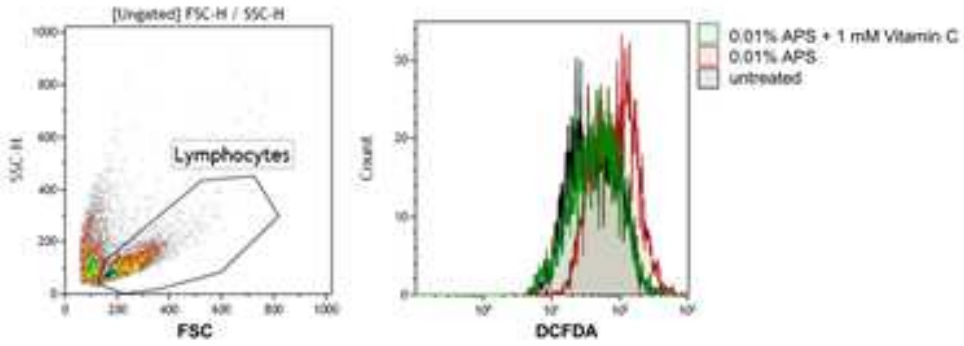

Ch VII S17 Figure 86 (2): Testing the specificity of DCFDA.

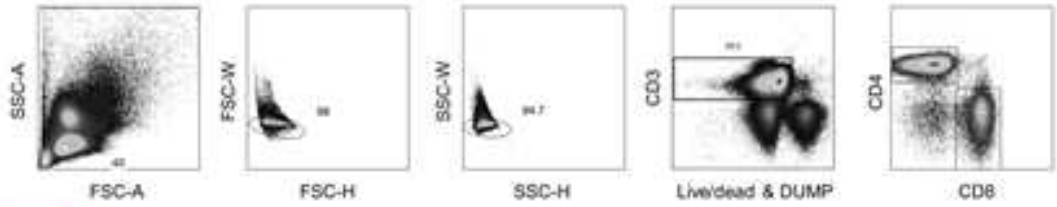

Ch VIII S1.1 Figure 87 (1). Gating of $CD4^+$ and $CD8^+$ T cells in peripheral blood.

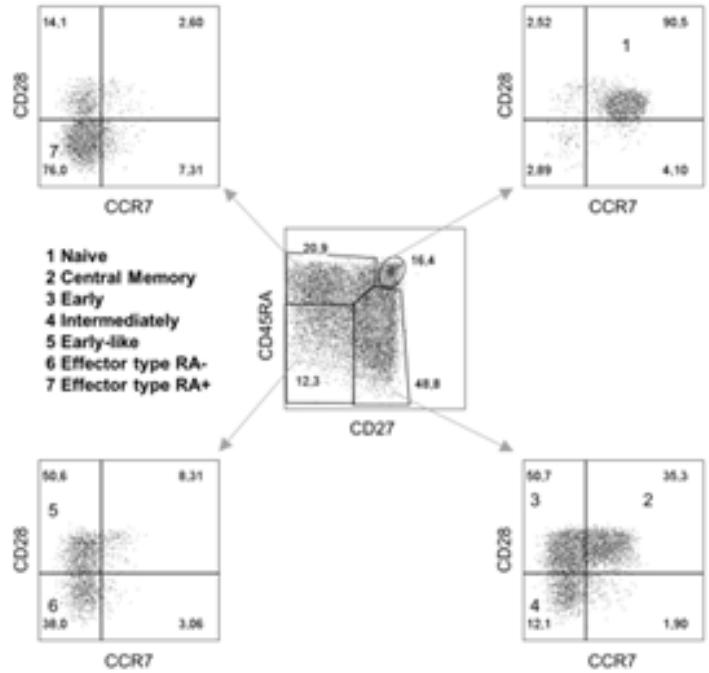

Ch VIII S1.1 Figure 88 (2). A four-dimensional model to address T-cell differentiation stages.

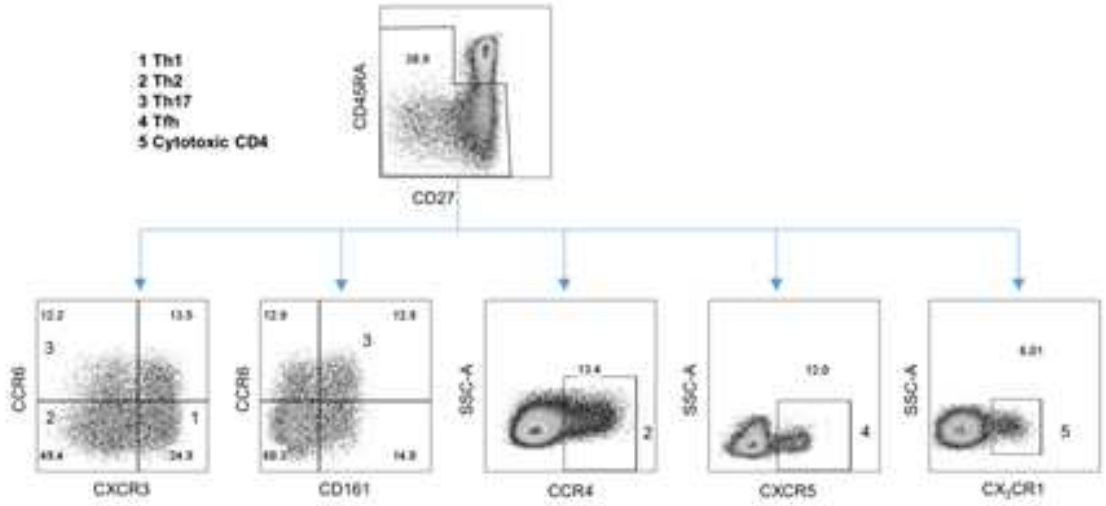

Ch VIII S1.1 Figure 89 (3). Adhesion and chemokine receptor expression identify four functional subsets within the human CD4^{+} memory pool.

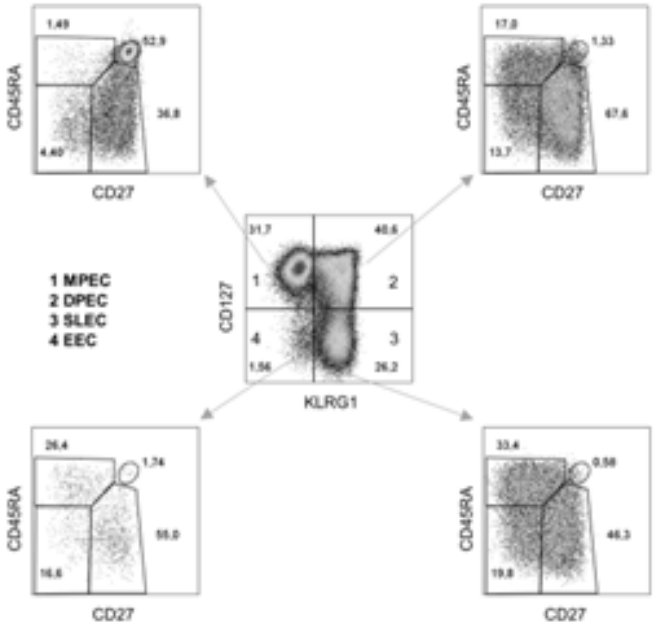

Ch VIII S1.1 Figure 90 (4). Effector CD8^{+} T-cell differentiation during acute infection using KLRG1 and CD127.

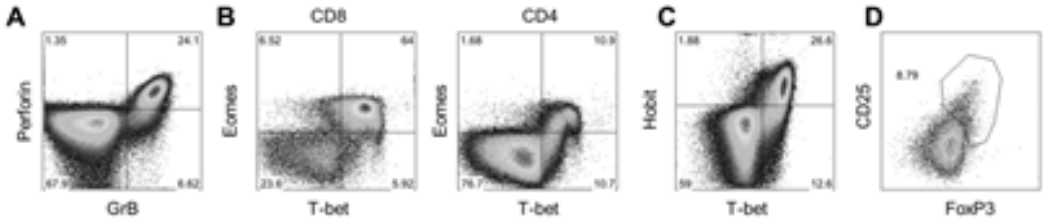

Ch VIII S1.1 Figure 91 (5). T-cell subsets as identified by intracellular cytokine and transcription factor staining.

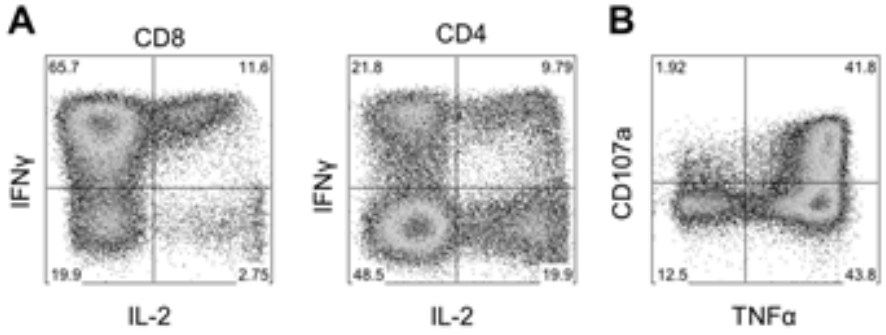

Ch VIII S1.1 Figure 92 (6). T-cell stimulation and visualization of antigen specific cells using MHC-tetramers.

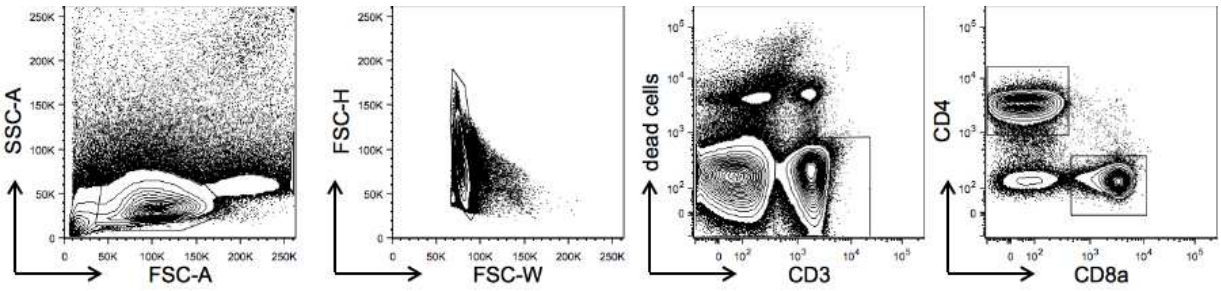

Ch VIII S1.2 Figure 93 (1): Gating on CD4 and CD8 T cells.

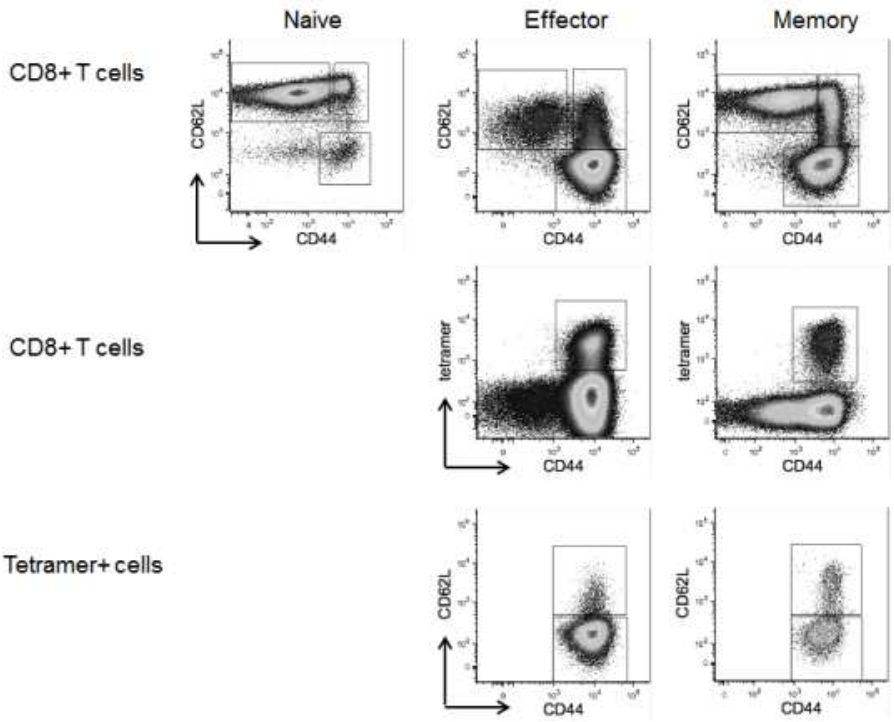

Ch VIII S1.2 Figure 94 (2): Discriminating naive, effector and memory T cells.

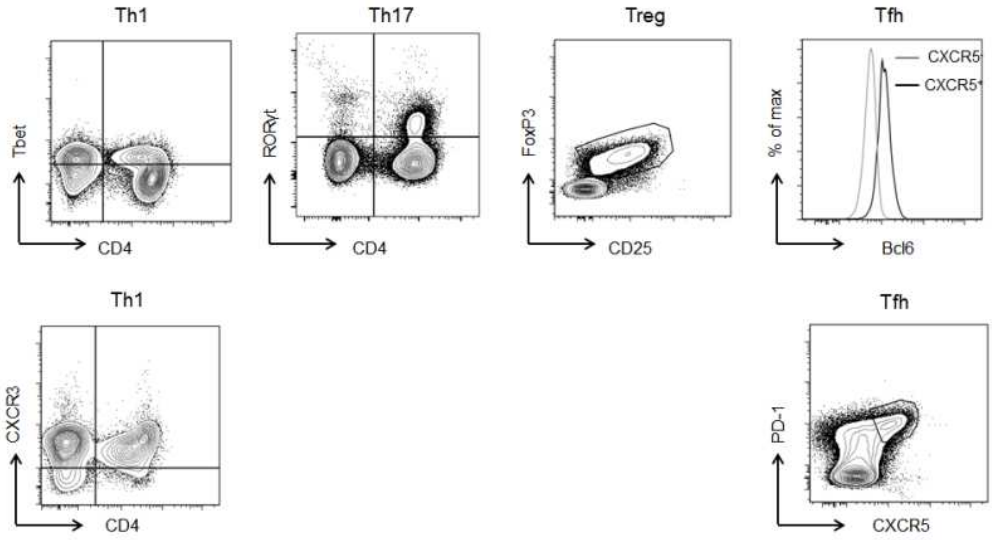

Ch VIII S1.2 Figure 95 (3): Using transcription factors or chemokine receptors to identify CD4 subsets.

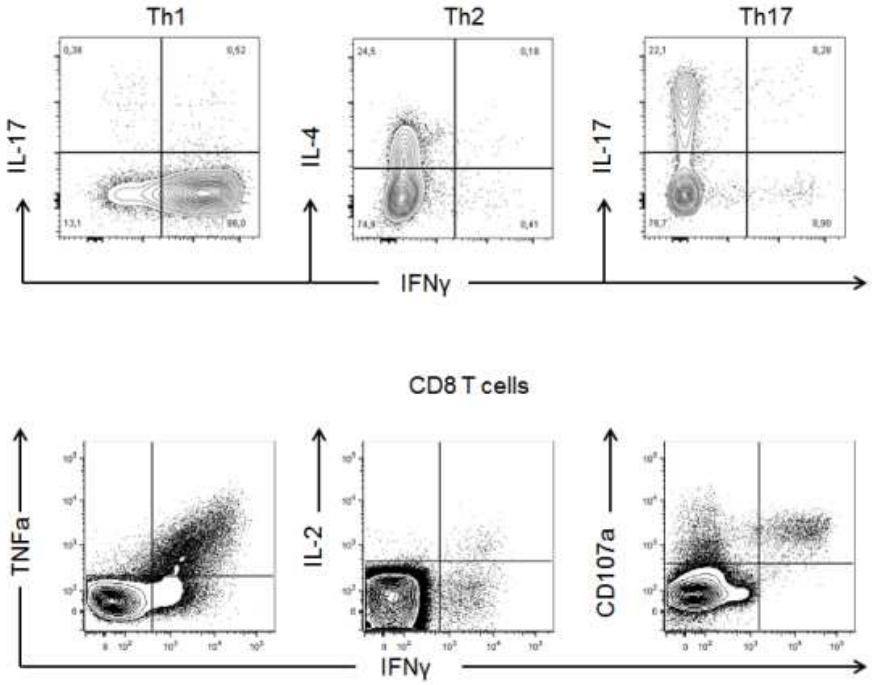

Ch VIII S1.2 Figure 96 (4): Effector molecules produced by T cells.

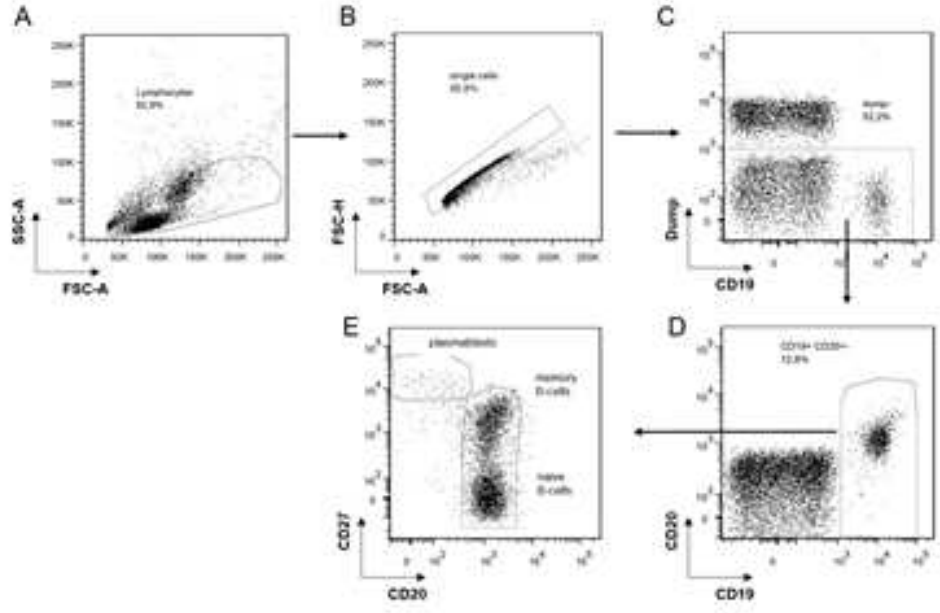

Ch VIII S2 Figure 97 (1): Gating strategy for the identification of B cells.

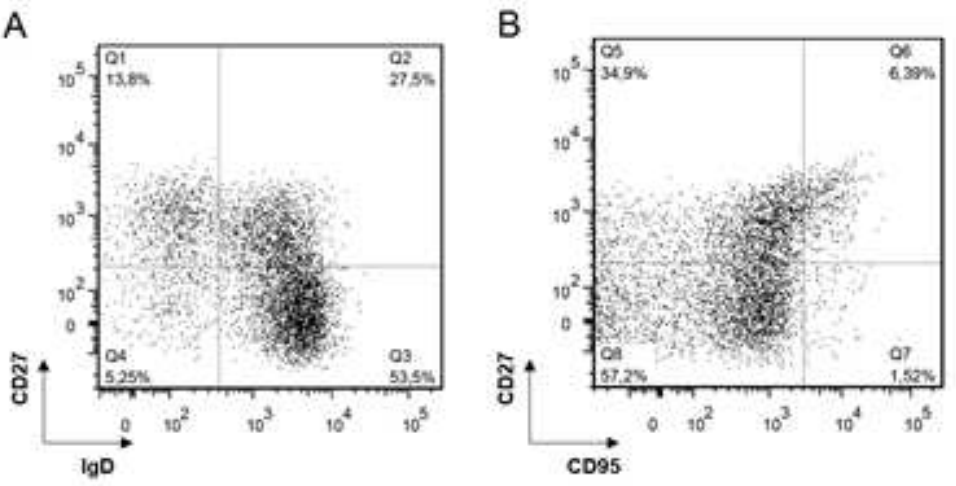

Ch VIII S2 Figure 98 (2): B-cell subsets.

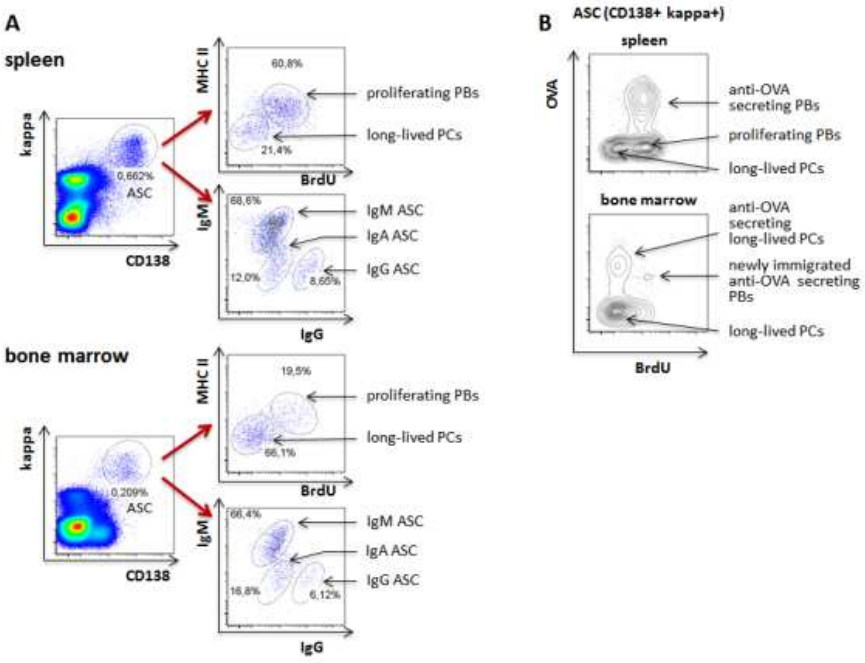

Ch VIII S3 Figure 99 (1): Flow cytometric analysis of murine ASC derived from spleen and bone marrow.

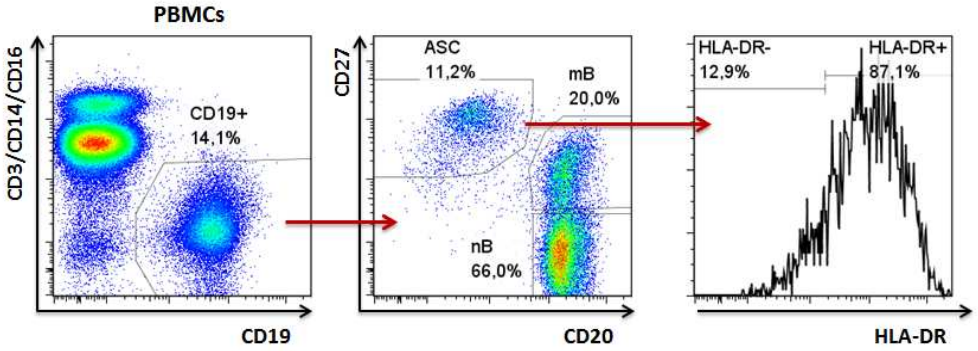

Ch VIII S3 Figure 100 (2): Flow cytometric analysis of circulating peripheral blood ASC derived from an active SLE patient.

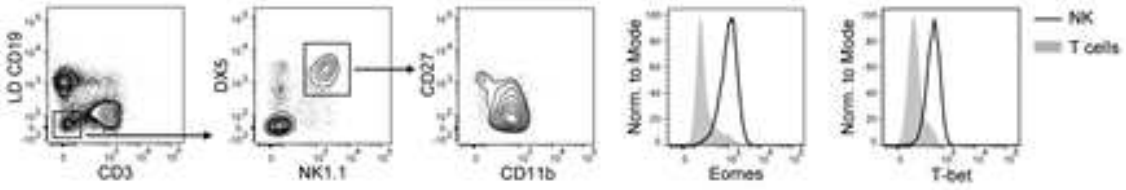

Ch VIII S4 Figure 101 (1). Identification of murine circulating splenic NK cells.

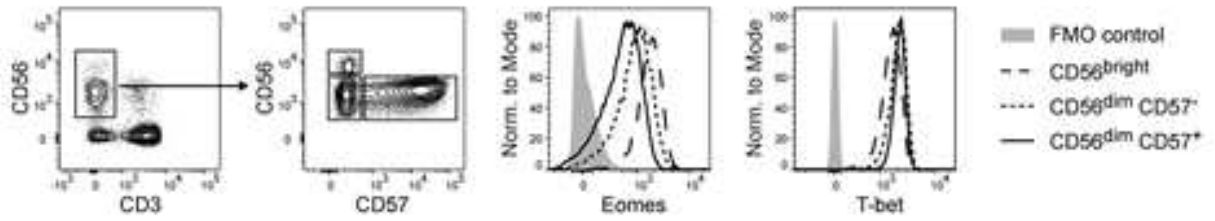

Ch VIII S4 Figure 102 (2): Identification of human circulating PB-NK cells.

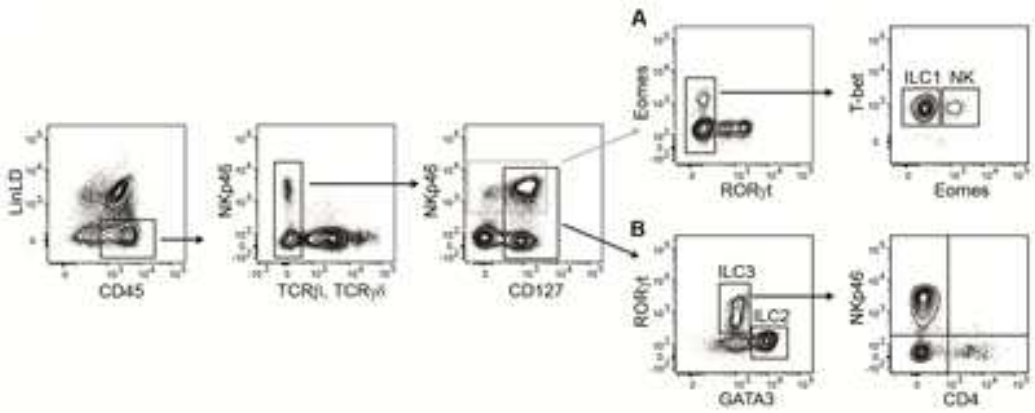

Ch VIII S4 Figure 103 (3). Identification of murine SI LP ILCs.

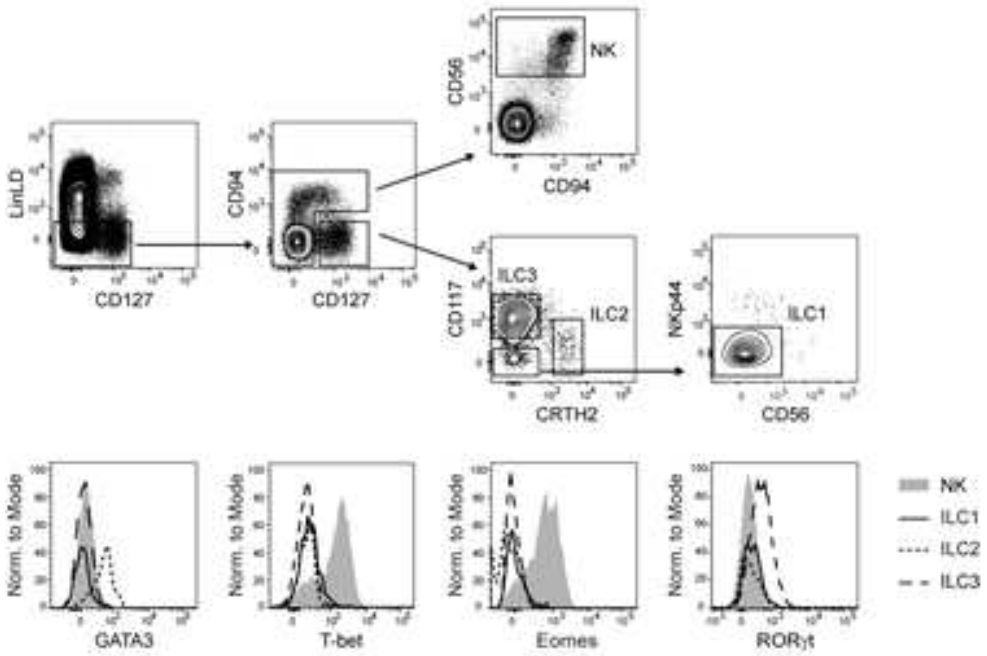

Ch VIII S4 Figure 104 (4): Identification of human tonsil ILCs.

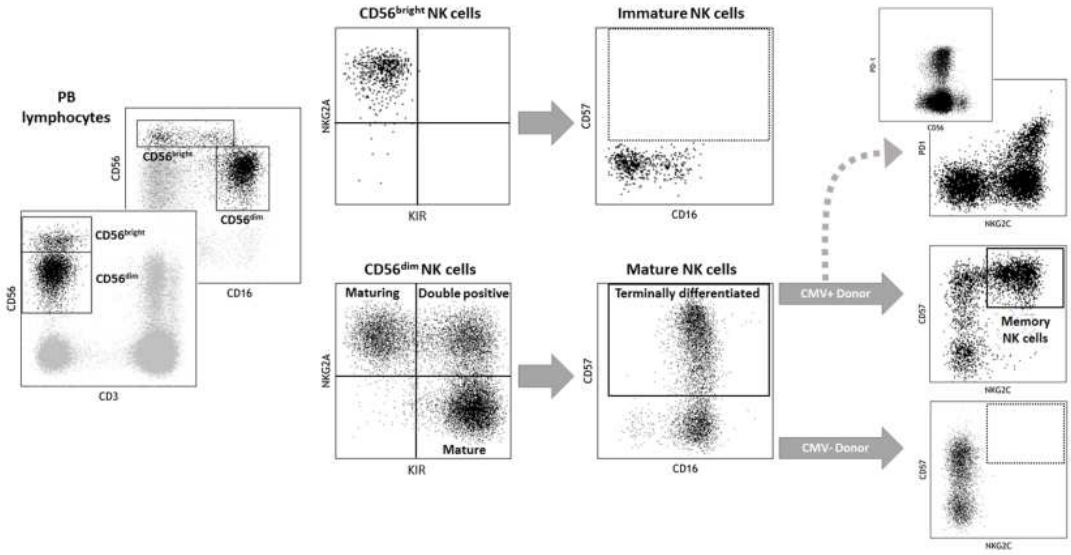

Ch VIII S5 Figure 105 (1): NK cells can be first gated on the basis of their surface level of CD56 expression and lack of CD3.

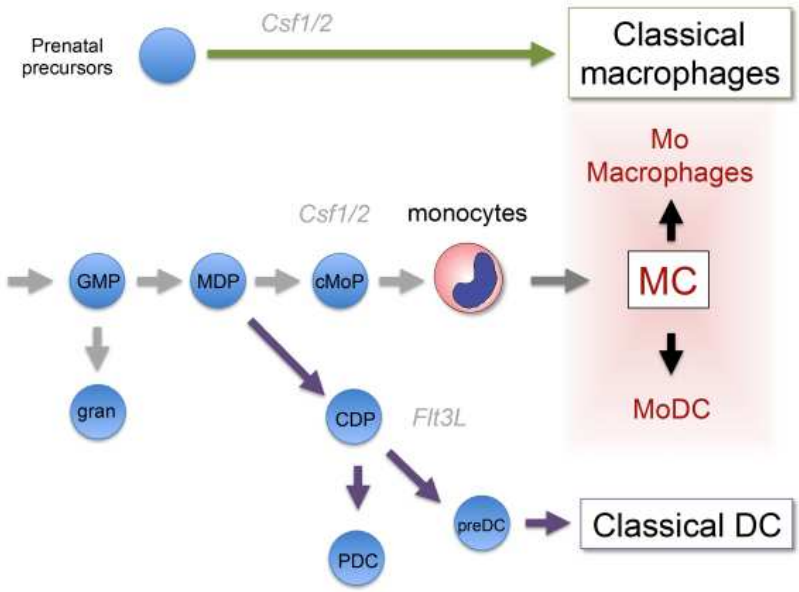

Ch VIII S6 Figure 106 (1). Schematic illustrating the tripartite organization of the mononuclear phagocyte system.

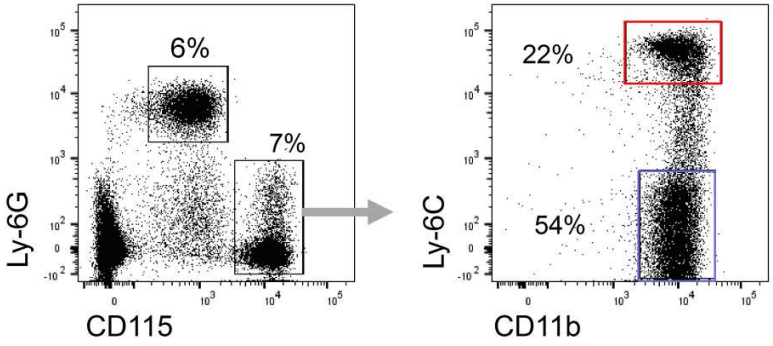

Ch VIII S6 Figure 107 (2). Flow cytometric analysis of murine myeloid blood cells.

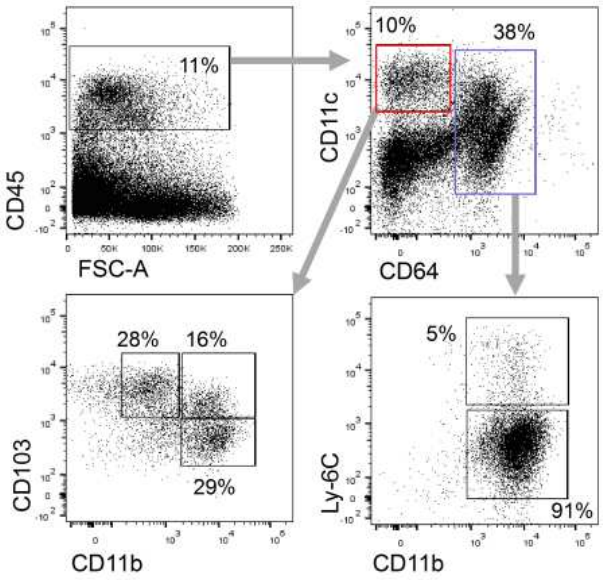

Ch VIII S6 Figure 108 (3). Flow cytometric analysis of colonic mononuclear phagocytes.

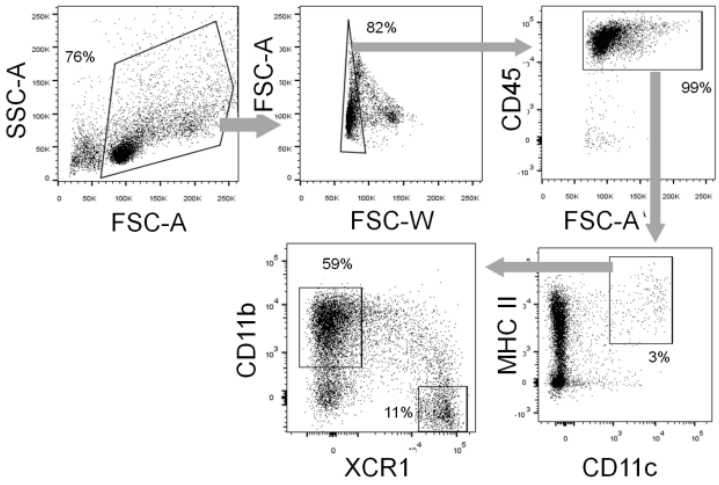

Ch VIII S6 Figure 109 (4). Flow cytometric analysis of splenic DCs.

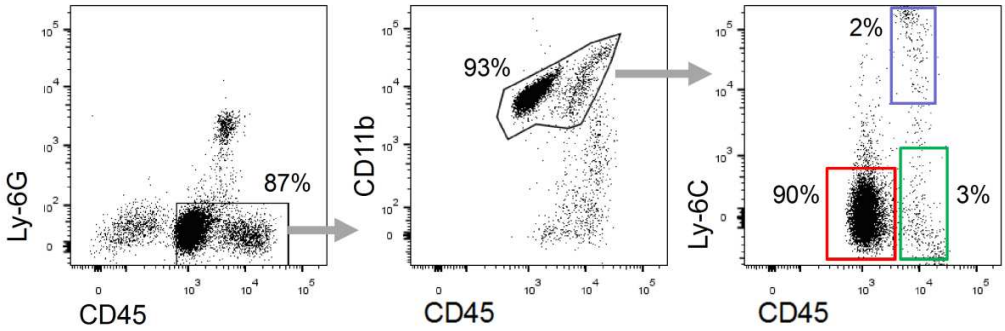

Ch VIII S6 Figure 110 (5). Flow cytometric analysis of CNS macrophages.

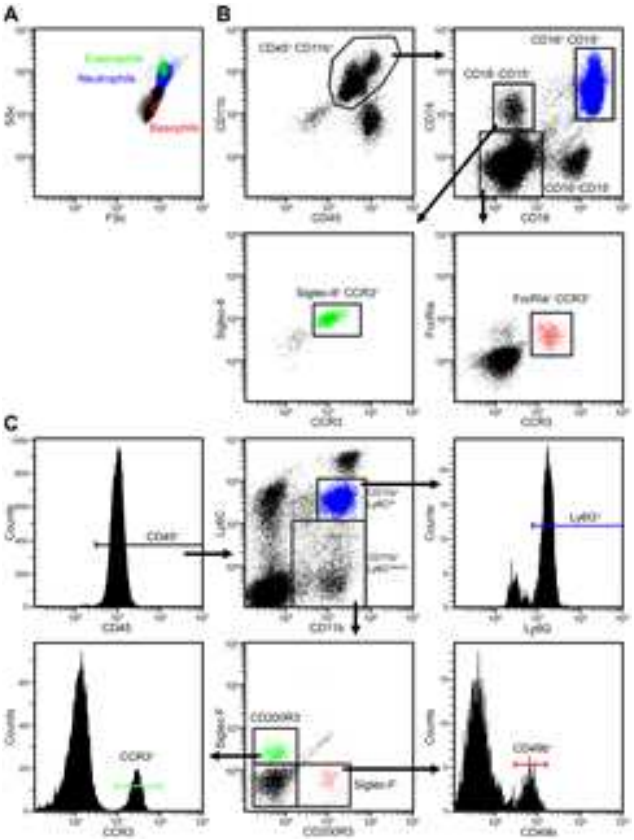

Ch VIII S7 Figure 111 (1). Discrimination of granulocyte subpopulations.

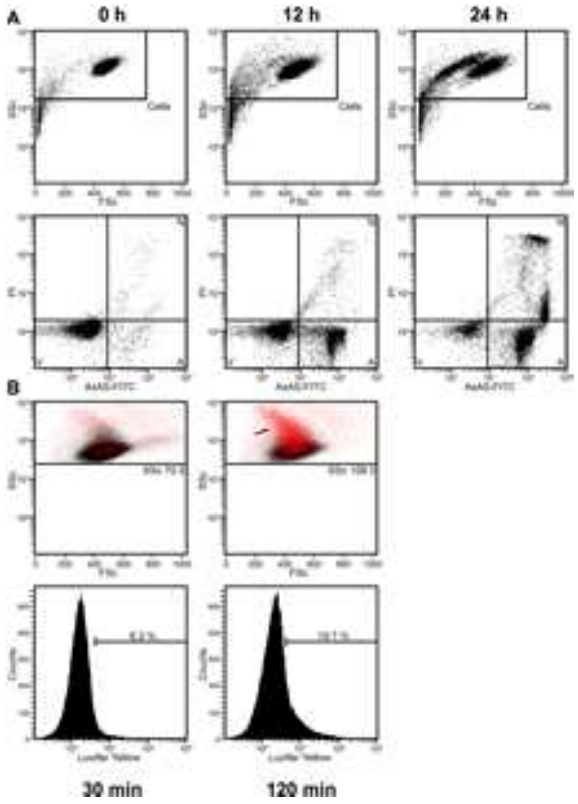

Ch VIII S7 Figure 112 (2). Apoptosis detection and uptake of nanoparticles in purified human granulocytes.

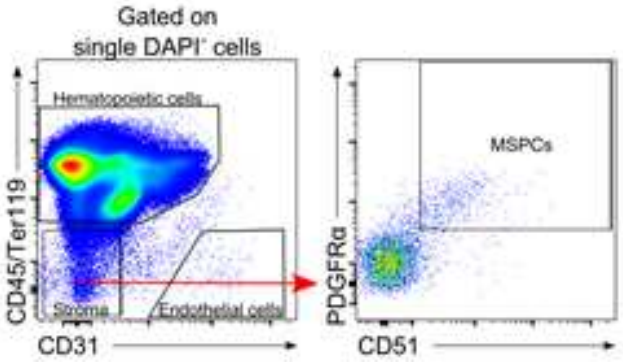

Ch VIII S8 Figure 113 (1). Gating strategy for bone marrow stromal cells

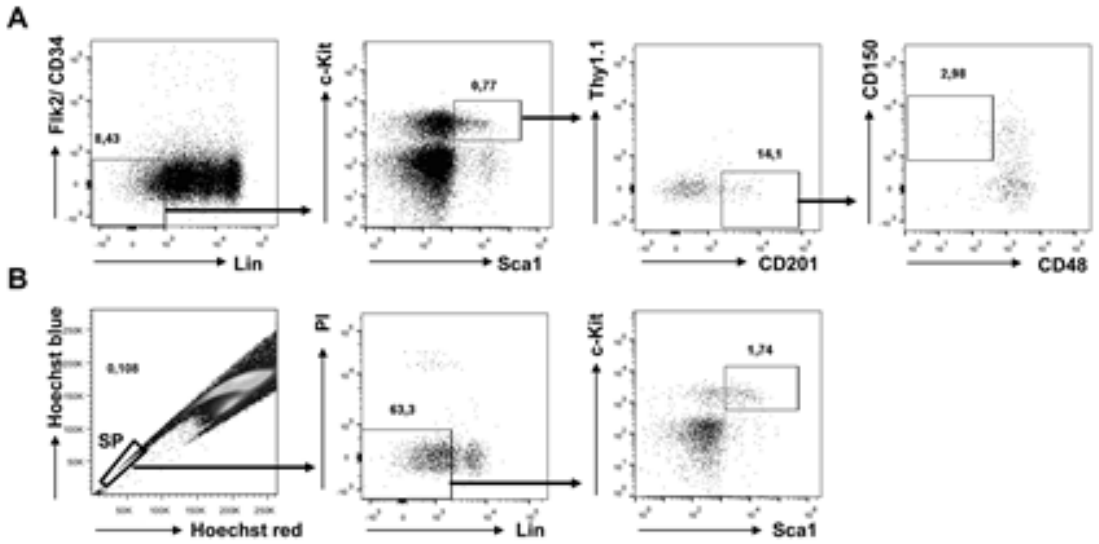

Ch VIII S9 Figure 114 (1). Phenotypic characterization of mouse HSCs in BM *in vivo*.

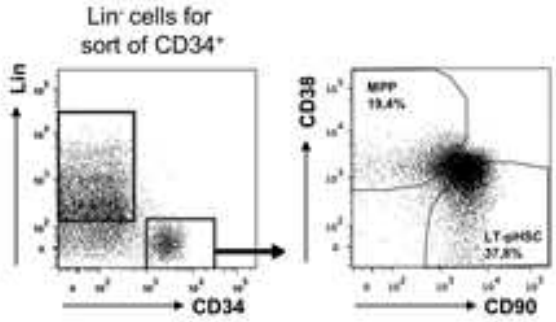

Ch VIII S9 Figure 115 (2). Phenotypic characterization of human pHSCs in the peripheral blood *in vivo*.